Transcriptomic landscape of mammalian ventral pallidum at single-cell resolution

Lite Yang[1,2], Lisa Z Fang[1], Michelle R Lynch[1,3], Chang S Xu[1,2], Hannah Hahm[1], Yufen Zhang[1], Monique R Heitmeier[1], Vincent Costa[5], Vijay K Samineni[1,2] *, Meaghan C Creed[1,2,4] *

1 Department of Anesthesiology, Washington University Pain Center, Washington University School of Medicine, St. Louis, MO, United States

2 Neuroscience Graduate Program, Division of Biology & Biomedical Sciences, Washington University School of Medicine, St. Louis, MO, United States

3 NINDS Neuroscience Postbaccalaureate Program, Washington University School of Medicine, St. Louis, MO, United States

4 Department of Psychiatry, Washington University School of Medicine, St. Louis, MO, United States

5 Oregon National Primate Research Center, Oregon Health and Science University, Portland, OR, United States

* Corresponding Authors: Meaghan C Creed – meaghan.creed@wustl.edu, Vijay K Samineni - vksamineni@wustl.edu

Keywords

Single nucleus RNA-seq, basal ganglia, mesolimbic, accumbens, dopamine

Abstract

The ventral pallidum (VP) is critical for motivated behaviors. While contemporary work has begun to elucidate the functional diversity of VP neurons, the molecular heterogeneity underlying this functional diversity remains incompletely understood. We used snRNA-seq and *in situ* hybridization to define the transcriptional taxonomy of VP cell types in mice, macaques, and baboons. We found transcriptional conservation between all three species, within the broader neurochemical cell types. Unique dopaminoceptive and cholinergic subclusters were identified and conserved across both primate species but had no homolog in mice. This harmonized consensus VP cellular atlas will pave the way for understanding the structure and function of the VP and identified key neuropeptides, neurotransmitters, and neuro receptors that could be targeted within specific VP cell types for functional investigations.

Introduction

The ventral pallidum (VP) is a hub within the ventral basal ganglia. The VP is the primary output of the ventral striatum and orchestrates activity of midbrain dopamine neurons and thalamic nuclei through direct and polysynaptic connections (*1*). The VP has been proposed to play the role of a 'limbic motor interface', regulating conditioned responses to appetitive and aversive stimuli. In rodents, manipulations of VP cellular activity produce profound effects on drug self-administration (*2–4*), decision making under conflict (*5–9*) and feeding (*10*, *11*). In humans, the VP is activated in response to reward-predictive cues (*12*) and the magnitude of this activation tracks the subjective and state-dependent value of rewards (*13*). Together, this points to the VP as a tractable brain target for neuromodulation therapies aimed at treating disorders of dysfunctional reward processing.

The VP was considered to be comprised primarily of inhibitory GABAergic neurons and neurons belonging to the basal forebrain cholinergic system (*14*). Contemporary circuit dissection, however, has revealed the VP also contains excitatory glutamatergic neurons. The projections of these glutamatergic neurons follow the same pathways as prototypical GABAergic neurons, but constitute a discrete population (*6*, *7*). These two populations, coarsely defined by whether they release glutamate or GABA, exert opposing effects on appetitive behavior with glutamatergic neurons constraining and GABAergic neurons promoting pursuit of rewards. Despite this functional heterogeneity, the molecular diversity within each of these neurochemically-defined subclasses remains poorly understood. Finally, our current understanding of the VP cellular makeup has been dissected along the expression of genes encoding transcription factors, calcium-binding proteins, or neurotransmitter receptors (i.e. parvalbumin [*Pvalb*], dopamine receptor D3 [*Drd3*] or neuronal PAS domain protein 1 [*Npas1*], *9*, *15*, *16*). Each of these broadly-defined populations was anatomically, biophysically, and functionally heterogeneous. Though these studies revealed valuable functional insights into the VP, they do not fully capture the cellular taxonomy of VP neurons. Thus, an overarching framework for understanding the molecularly-defined cell types within the VP, and thus for integrating these prior circuit-level studies into an overarching model of VP function, is lacking.

Given its role in modulating reward evaluation, seeking, consumption, and associative learning, many circuit dissection studies have proposed the VP to be a target for therapies for mental and emotional disorders. A key first step towards translation is determining whether cell types under investigation in rodents are conserved in primate species. As in rodent studies (*5*, *17–21*), *in vivo* recording in primates during reward-guided choice assays reveals that response profiles of VP neurons to rewards and reward-predictive cues are heterogeneous, and VP neuronal firing reflects discrete attributes of rewards and operant responding (*22–25*). However, the cellular diversity of the VP has not been characterized in non-rodent species. Given the difficulty in obtaining high-quality human samples and the evolutionary proximity of non-human primates (NHPs) to humans, old world monkeys are an ideal model organism for understanding principles governing transcriptomic profiles of basal ganglia neurons. Here, we performed single-nucleus RNA sequencing (snRNA-seq) of the VP across one rodent and two primate species, macaques (*Macaca mulatta*) and baboons (*Papio anubis*), followed by spatial validation of identified VP cell types. The transcriptional taxonomy presented here emphasizes the conserved nature of VP cell types across mammalian species and lays a foundation for understanding how the activity of these cell types modulates reward-guided behavior.

Results

Mouse atlas of ventral pallidum

To profile the transcriptional diversity of VP neurons, we performed snRNA-seq on four VP samples (two female and two male samples, Fig. 1A, Methods). After quality control and removal of low-quality nuclei and doublets, 38,130 nuclei were retained in the final dataset with an average of 2,105.7 genes per nucleus (Fig. S1A, Table S1). Notably, nuclei from individual libraries were represented in each cluster, indicating a low level of technical variation (Fig. S1B). Clustering analysis revealed eight major

transcriptional cell types including neurons (65.2% of the total nuclei), astrocytes (10.8%), choroid epithelial cells (0.2%), macrophages (0.1%), microglia (4.5%), oligodendrocytes (12.3%), oligodendrocyte progenitor cells (OPC, 5.4%), and vascular cells (1.5%; Fig. 1B). These cell types exhibit distinct transcriptional profiles and are marked by high expression levels of canonical marker genes of each type (Fig. 1C, Table S2; *26*, *27*).

Among all transcriptional cell types, neurons exhibited a high degree of transcriptional heterogeneity based on inspection of the UMAP (Fig. 1B). Unsupervised clustering of the neuronal nuclei revealed 20 neuronal clusters, including 16 GABAergic clusters (90.1% of neuronal nuclei) with distinct expression of canonical marker genes (i.e. *Slc32a1* encoding vesicular GABA transporter [VGAT], *Gad1*, and *Gad2*) and four glutamatergic clusters (9.9%) labeled with distinct expression of *Slc17a6*, *Slc17a7, or Slc17a8* encoding vesicular glutamate transporter (VGLUT) isoforms 2, 1, and 3, respectively (Fig. 1D,E, Fig S1C). One of the glutamatergic clusters is also cholinergic (1.5%) based on the expression of *Chat*. Within each of those neurochemical subclasses, neuronal clusters exhibit distinct transcriptional profiles and thus we named them by a combination of marker genes that uniquely labeled each cluster (Fig. 1E, Fig. S1C, Table S2, Methods).

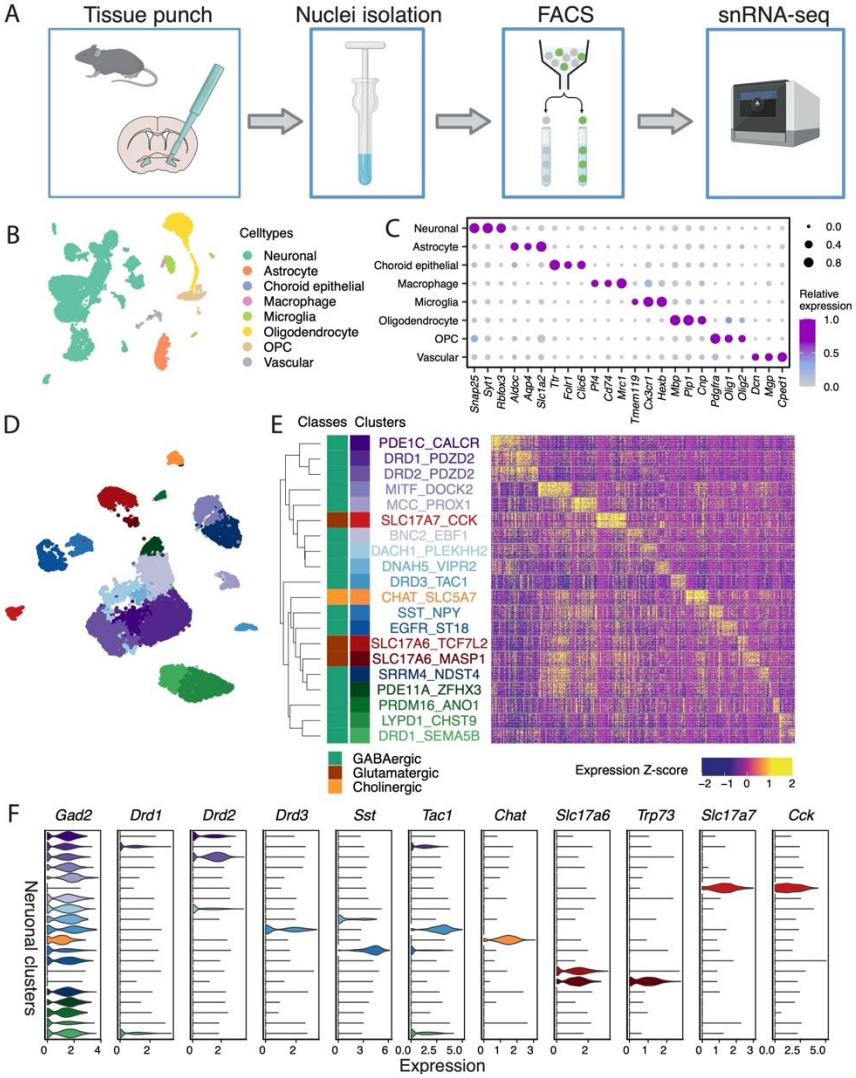

Fig. 1. Mouse atlas of ventral pallidum. (**A**) Experimental workflow of snRNA-seq of mouse VP. (**B**) Uniform manifold approximation and projection (UMAP) visualization of 10,000 downsampled nuclei, colored by cell types. (**C**) Dot plot displaying the expression of select cell-type-specific marker genes in individual cell types. Dot size denotes the fraction of nuclei expressing a marker gene (>0 counts), and color denotes relative expression of a gene in each cell type (calculated as the mean expression of a gene relative to the highest mean expression of that gene across all cell types). (**D**) UMAP of 10,000 downsampled mouse neuronal nuclei, colored by neuronal clusters. (**E**) Heatmap showing Z-scores of the expression of top 100 marker genes (sorted by Log2FC) per neuronal clusters in individual nuclei of snRNAs-seq. 50 nuclei are downsampled per neuronal cluster and displayed on the heatmap. Neuronal clusters are ordered based on the hierarchical clustering of the expression of marker genes displayed on the heatmap. The color bars on the side denote neuronal classes and clusters. (**F**) Violin plot showing log-transformed expression of select marker genes in individual neuronal clusters. Neuronal clusters are ordered according to the dendrogram in E.

We identified 16 clusters of GABAergic neurons in the mouse VP, many of which corresponded to the GABAergic neurons previously described in basal forebrain structures (*26*, *28*, *29*). GABAergic neuronal clusters were differentiated based on enrichment of genes encoding neuropeptides (i.e. *Sst*, *Tac1*), neurotransmitter receptors (i.e. *Calcr*, *Vipr2*, dopamine receptors, *Drd1*, *Drd2*, *Drd3)*, and/or transcription factors implicated in cell fate determination and neural differentiation (i.e. *Lypd1*, *Dach1*, *Mitf*, *Prox1*, *Ebf1*, *Zfhx3*, *Prdm16*, *Srrm3*). Three clusters of GABAergic neurons (PDE1C_CALCR, DRD1_PDZD2, AND DRD2_PDZD2) were hierarchically organized into dendrograms based on transcriptional similarity and characterized by the highest expression level of *Pdzd2*, a gene encoding for a PDZ-domain containing protein previously used as a marker of striatal cell types (*26*). Using publicly available data, we confirmed dense expression of *Pdzd2* in the VP immediately ventral to the anterior commissure, and sparser

expression in more ventral territories of the VP, arguing against the classification of *Pdzd2*-expressing neurons as strictly belonging to ventral striatum (Fig. S2; *28*, *29*).

We also characterized four glutamatergic clusters (based on the expression of one of the three isoforms of VGLUT), one of which represents neurons of the basal forebrain cholinergic system (CHAT_SLC5A7), with distinct expression *Slc17a8* (VGLUT3) as previously reported (Fig. S1C; *32*). We also identified a sparse but discrete population of *Slc17a7* (VGLUT1)-expressing neurons (SLC17A7_CCK), which nearly exclusively co-localized with *Cck* that encodes neuropeptide cholecystokinin, analogous to neuronal subpopulations previously described in the extended amygdala (*33*, *34*). Finally, our clustering revealed two distinct populations of *Slc17a6* (VGLUT2)-expressing neurons in the mouse VP (SLC17A6_TCF7L2 and SLC17A6_MASP1; Fig. 1D,E). Substantial prior work has demonstrated these *Slc17a6*-positive VP neurons are largely non-overlapping with GABAergic populations (*6*, *7*), which we confirm. Our results comport with publicly available MERFISH datasets (*28*, *29*) confirming the presence of two *Slc17a6*-positive neuronal populations throughout the basal forebrain. *Slc17a6*-positive VP neurons were differentiated by their expression of *Trp73*, which was expressed exclusively in the minor *Slc17a6*-positive cluster SLC17A6_MASP1 (Fig. 1F; *28*, *29*).

VP activity is necessary for sex-specific parenting behavior (*35*), and sex differences in peptidergic inputs to the VP have been reported (*36*). Therefore, we next asked if the VP showed sex-specific differences in cell type composition and gene expression. Analysis revealed that male and female VPs contain broadly the same cell types (Fig. S1D) that express highly similar marker genes (Pearson's r = 0.92 - 0.99 per neuronal cluster/cell type between males and females (Fig. S1E). We next compared transcriptional profiles of nuclei of distinct VP neuronal clusters or non-neuronal cell types between sex. Differential gene expression analysis revealed 237 genes that are significantly (Log2FC > 0.5, FDR < 0.05) more highly expressed in males and 139 genes that are more highly expressed in females (Fig. S1F, Table S3). The most dramatic sex differences in gene expression are known sex-specific genes involved in X inactivation (e.g., *Xist*, *Tsix*) that are more highly expressed in females or Y chromosome genes (e.g., *Uty*, *Ddx3y*) that are more highly expressed in males. In addition to known sex-specific gene expression, *Ttr*, which encodes a thyroid hormone (TH) transporter transthyretin, is expressed more highly in several neuronal clusters of male mice, which may underlie sex-specific neurochemical and morphological alterations(*37*). In addition, *Htr1f,* encoding 5-hydroxytryptamine (serotonin) receptor 1F, is more highly expressed in neuronal clusters DRD1_PDZD2 and DRD2_PDZD2 of female mice, suggesting a potential functional role in a sex-specific manner.

<u>Spatial validation of select transcriptional clusters</u>

To corroborate the expression of marker genes for select VP neuronal clusters and to visualize the spatial location of these clusters across the VP, we performed HiPlex FISH in mouse tissue. We prioritized canonical VP marker genes that also distinctly label subsets of VP neurons (*Cck, Chat, Slc17a6, Trp73, Gad2, Tac1, Drd1, Drd2, Drd3, Sst*; Fig. 2A,B), and detected their distribution along the anterior-posterior axis of the VP. In total 2,779 nuclei expressing at least one of the marker genes were segmented from images taken across four coronal sections representing the anterior to posterior extent of the VP. The anatomical coordinates of nuclei were then reconstructed (Fig. 2C) and compared to our snRNA-seq results to corroborate the expression of the identified cell types in the VP. We were able to validate and discover the topographical organization for many neuronal clusters, represented across the anterior-posterior, medio-lateral, and dorsal-ventral extents of the VP. Consistent with the snRNA-seq, GABAergic neurons are highly enriched in the VP, whereas *Slc17a6*-positive cells are present in fewer nuclei with often widely dispersed. The GABAergic cluster labeled by *Drd3* and *Tac1* exhibited a medio-lateral bias and were concentrated along the lateral portions of the VP. Our analysis also revealed that the majority of this cluster localized in the mid- region in the anterior-posterior axis, while *Sst*-positive neurons were concentrated in the most posterior extent of the VP (Fig. 2D). The two identified *Slc17a6*-positive clusters comport with publicly available MERFISH datasets; the SLC_MASP1 minority cluster is distinguished from the SLC_TCF7L2 majority cluster by exclusive expression of *Trp73*. Neurons co-expressing *Slc17a6* and *Trp73* showed a more medial distribution relative to *Slc17a6*-positive neurons that did not co-express *Trp73* (Fig. 2C). Consistent with prior work, *Chat*-positive cholinergic neurons were distributed sparsely

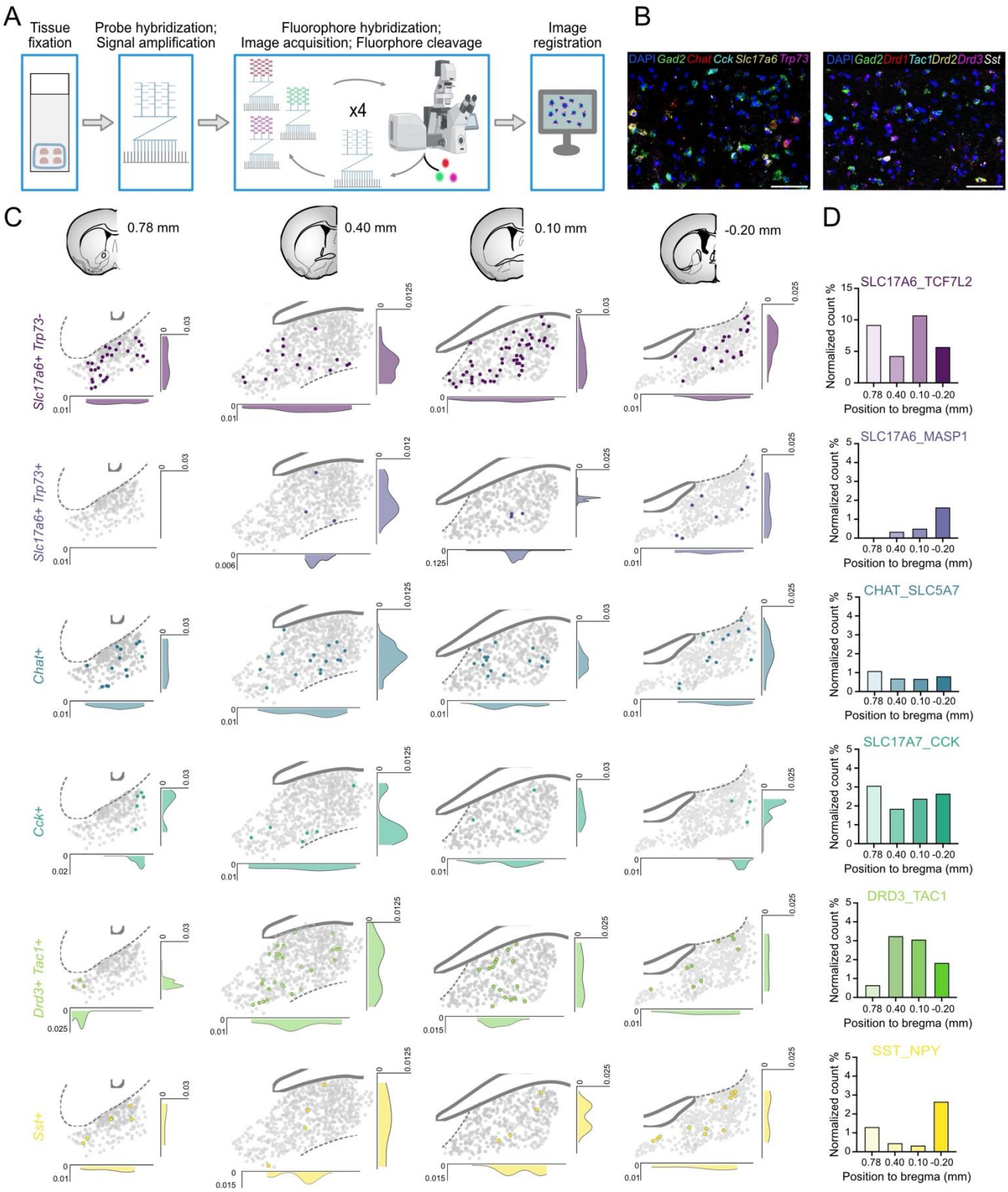

Fig. 2. Spatial organization of transcriptionally-distinct mouse clusters. (**A**) Experimental workflow of HiPlex FISH in mouse VP. (**B**) Representative HiPlex FISH images showing select probes for marker genes used to differentiate specific neuronal clusters. DAPI was used as a counterstain. Left: Probes hybridized to *Gad2*, *Chat*, *Cck*, *Slc17a6*, and *Trp73* mRNA. Right: Probes hybridized to *Gad2*, *Drd1*, *Tac1*, *Drd2*, *Drd3*, and *Sst* mRNA. Scale bar = 50 µm. (**C**) Spatial maps of neuronal clusters SLC17A6_TCF7L2, SLC17A6_MASP1, CHAT_SLC5A7, SLC17A7_CCK, DRD3_TAC1, and SST_NPY over four levels of the VP. Gene markers used to detect clusters are indicated to the left. Colorized dots represent cells that expressed marker genes for each specified cluster, while gray dots represent cells that did not express these marker genes. Density plots depict the relative distribution of cells in individual clusters over the mediolateral and dorsoventral extent of the VP. (**D**) Bar graphs indicating the proportion of cells belonging to individual clusters over the anteroposterior axis of the VP. Counts for cells in each cluster were normalized to the total neurons detected during HiPlex FISH at each level and expressed as a percentage.

throughout the VP, similar to adjacent basal forebrain structures (*28*, *29*). Dopaminoceptive neurons (expressing the dopamine receptors *Drd1, Drd2,* and *Drd3*) spanned the extent of the VP, without obvious functional gradients or clear borders of expression (Fig. S4). Finally, immunohistochemistry corroborated the relative expression and general distribution of neuronal and non-neuronal classes determined by snRNA-seq in our mouse samples (Fig. S3).

NHP atlases of ventral pallidum

The basal ganglia are highly conserved throughout vertebrates, yet the cellular composition of the VP remains largely unexplored in species other than rodents. As NHPs exhibit evolutionary similarity to humans, they serve as an optimal model organism for bridging the gaps between rodent and human studies and unraveling the underlying principles governing the transcriptomic profiles of basal ganglia neurons. We performed snRNA-seq on four biological samples of three macaques and four biological samples of two baboons. We first conducted independent quality control and clustering analysis for each species (Table S1). The baboon dataset contains 57,724 high-quality nuclei with an average sequencing

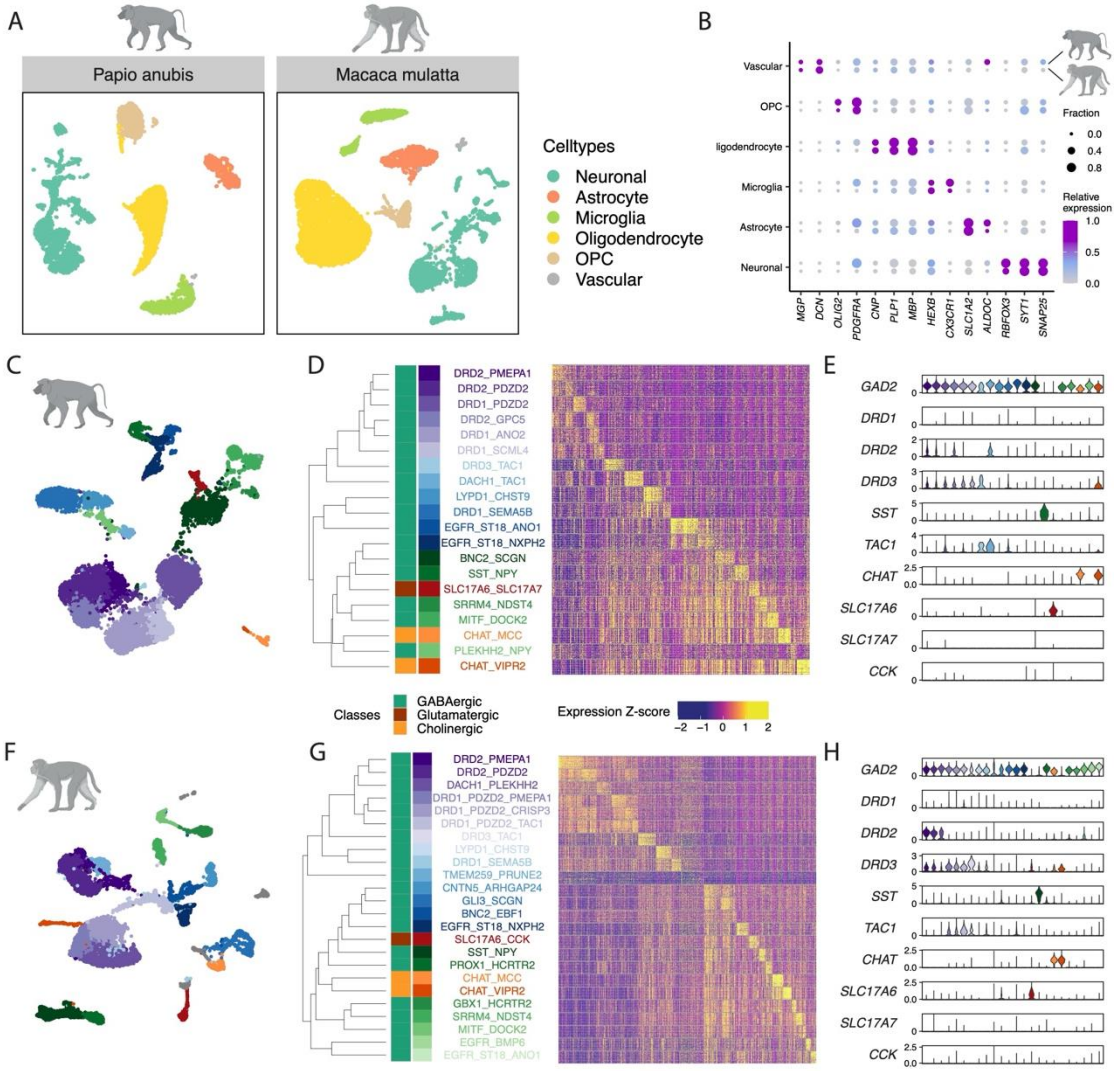

Fig. 3. Non-human primate atlas of ventral pallidum. (**A**) UMAP visualization of 10,000 downsampled nuclei each from baboon and macaque, colored by cell types. (**B**) Dot plot displaying the expression of select cell-type-specific marker genes in individual cell types from baboon and macaque. Dot size denotes the fraction of nuclei expressing a marker gene (>0 counts), and color denotes relative expression of a gene in each cell type (calculated as the mean expression of a gene relative to the highest mean expression of that gene across all cell types in the respective species). (**C** and **F**) UMAP of 10,000 downsampled neuronal nuclei from baboon (C) and macaque (F), colored by neuronal clusters. (**D** and **G**) Heatmap showing Z-scores of the expression of top 100 marker genes (sorted by Log2FC) per neuronal clusters in individual nuclei from baboon (D) and macaque (G). 50 nuclei per neuronal cluster are downsampled and displayed on the heatmap for each species. Neuronal clusters are ordered based on the hierarchical clustering of the expression of marker genes displayed on the heatmap. The color bars on the side denote neuronal classes and clusters. (**E** and **H**) Violin plot showing log-transformed expression of select marker genes in individual baboon (E) and macaque (H) neuronal clusters. Neuronal clusters are ordered according to the dendrogram in D and G, respectively.

depth of 2,030.4 genes per nucleus (Fig. S5A) and the macaque dataset contains 49,542 high-quality nuclei with an average sequencing depth of 2,269.6 genes per nucleus (Fig. S5B). To identify transcriptionally distinct cell types, we first performed independent clustering of the snRNA-seq data from each species. In both macaque and baboon VP atlases, we identified six cell types including neurons (27.7% of total macaque nuclei, and 28.2% of total baboon nuclei), astrocytes (9.4% and 6%), microglia (11.8% and 15.4%), oligodendrocytes (41.8% and 37.3%), OPCs (8.7% and 12.9%), and vascular cells (0.6% and 0.2%; Fig. 3A). These cell types exhibit high expression levels of previously reported canonical marker genes (Fig. 3B), which were largely conserved between the two NHPs and mice. We also observed proportionally fewer neuronal nuclei in both NHP atlases compared to the mouse atlas, consistent with previous reports (*38*–*43*).

Neuronal nuclei in each NHP species displayed high levels of transcriptional heterogeneity, which is homologous to the mouse VP atlas. To better understand the transcriptional heterogeneity of NHP VP neurons, we performed independent subclustering of the neuronal nuclei from each species. In baboon, we identified 20 neuronal clusters including 17 GABAergic clusters (97.3% of the neuronal nuclei) and three glutamatergic clusters, two of which are also cholinergic (Fig. 3C,D). In macaque, subclustering revealed 24 neuronal clusters including 21 GABAergic clusters (93.4% of the neuronal nuclei) and three glutamatergic clusters, two of which are cholinergic (Fig. 3F,G). Those neuronal clusters were differentiated based on specifically enriched genes, many of which are conserved across all species. Clusters of GABAergic neurons from NHPs expressing high level of *PDZD2* were hierarchically organized based on transcriptional similarity, consistent with the observation in the mouse atlas. While *PDZD2* is expressed in all neuronal clusters, it is expressed highly in an expanded population in NHPs (six clusters constituting 58.8% of neuronal nuclei in baboon, seven clusters constituting 50.2% of total nuclei in macaque) compared to mouse (three clusters constituting 32.9% of the neuronal nuclei; Fig. S1C, S5G,H).

We identified three glutamatergic clusters expressing one of the three isoforms of the vesicular glutamate transporters. We identified two cholinergic clusters (CHAT_MCC and CHAT_VIPR2) in both baboon and macaque, which distinctly express *SLC17A8* (VGLUT3; Fig. S5G,H; *32*). We also identified a distinct population of *SLC17A6* (VGLUT2)-positive neurons in NHPs (SLC17A6_SLC17A7 baboon, SLC17A6_CCK macaque). While neurons of this cluster exclusively co-localized with *CCK* in the two NHP species, *SLC17A7* (VGLUT1) is uniquely expressed in baboons (Fig. 3D,E, Fig. S5G), but not in macaques (Fig. 3G,H, Fig. S5H).

Despite largely conserved marker genes that identify NHP and mouse VP neuronal clusters, there is a species-specific diversification of these neuronal subtypes. Macaque and baboon VP datasets revealed lower transcript detection of *DRD1*, *SLC17A7,* and *CCK*, and higher detection of *DRD3* relative to the mouse VP atlas. We also observed that *TAC3* is highly expressed in neuronal cluster EGFR_ST18_NXPH2 in macaque and baboon VP atlases while it is absent from all cell types in the mouse VP (Fig S3 G,H), consistent with previous report of primate-specific *TAC3* expression in cortical and striatal interneurons (*42*). Overall, we identified distinct VP cell types that are conserved across macaque and baboon, and based on their marker gene expression, the VP transcriptional landscapes are largely shared across species.

<u>Harmonized cross-species atlas of ventral pallidum identifies conserved neuronal populations</u>

To take full advantage of the cross-species information and examine the correspondence of transcriptional cell types, we generated a harmonized atlas by integrating the neuronal nuclei from snRNA-seq data across all three species (*44*). Integration matched shared cell types across species as nuclei of the same major neuronal classes show extensive intermingling on the integrated UMAP compared to complete separation on the UMAP pre-integration (Fig. 4A, S6A). We next performed clustering of this harmonized neuronal atlas and generated 26 integrated clusters (Fig. S6B).

To identify neuronal cell types that are evolutionarily conserved, we first examined the integrated clusters that showed a high degree of correspondence to individual neuronal clusters from each of the species

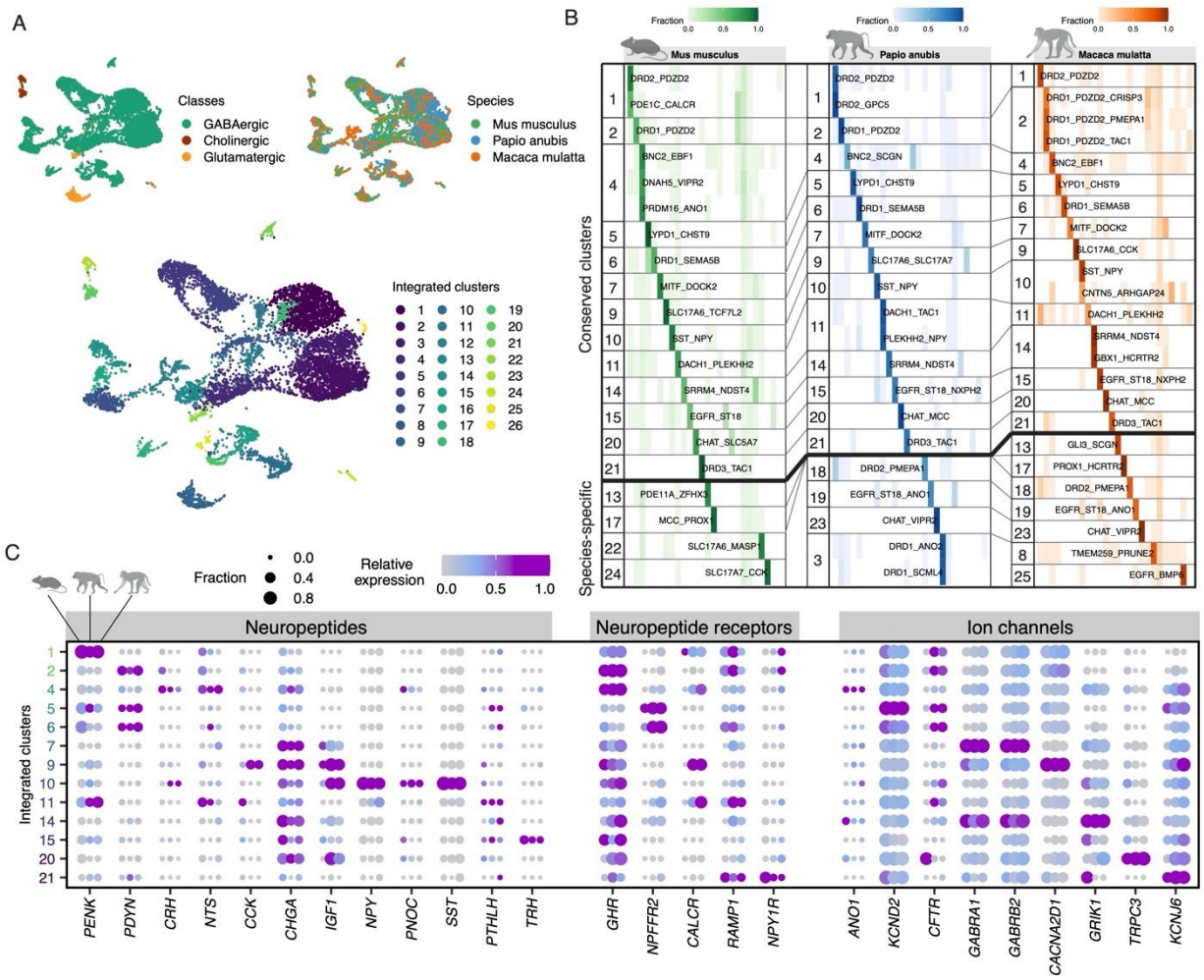

Fig. 4. Harmonized cross-species atlas of ventral pallidum neurons. (**A**) UMAPs of the harmonized neuronal atlas of VP. 3,000 neuronal nuclei per species are downsampled from mouse, baboon, and macaque. Nuclei are colored by neuronal cell types (top left), species (top right), and integrated clusters from the harmonized atlas (bottom). (**B**) Heatmap showing the correspondence of neuronal clusters across species. Fraction of nuclei in each neuronal cluster defined by independent analysis for each species that mapped to each integrated cluster identified in the harmonized atlas is calculated. Integrated clusters consisting of nuclei that made up over 30% of the nuclei from at least one neuronal cluster per species are considered conserved clusters. All other integrated clusters are identified as species-specific. (**C**) Dot plot displaying the expression of select gene panels in individual cell types from mouse, baboon, and macaque. Dot size denotes the fraction of nuclei expressing a marker gene (>0 counts), and color denotes relative expression of a gene in each cell type (calculated as the mean expression of a gene relative to the highest mean expression of that gene across all cell types in the respective species).

characterized by independent analysis. We identified 13 clusters in the integrated atlas that each had at least one corresponding neuronal cluster in every species (Integrated clusters 1, 2, 4, 5, 6, 7, 9, 10, 11, 14, 15, 20 and 21, Fig. 4B, S6C, Methods). Compared to all other neuronal clusters identified based on independent analysis, neuronal clusters of different species within a conserved cluster exhibit significantly higher transcriptional similarity with respect to the expression of conserved marker genes (Pearson's r = 0.87 ± 0.12 among neuronal clusters in the same integrated clusters, compared to Pearson's r = 0.62 ± 0.11 among neuronal clusters not in the same integrated clusters, p = 3.94e-63, two-sided student t-test; Fig. S6D). Many of these conserved clusters are identified by genes encoding neuropeptides or neuropeptide receptors, i.e. DRD2_PDZD2, DRD2_GPC5, DRD1_PDZD2, DRD1_SEMA5B, SST_NPY, CHAT, DRD3_TAC1 (Fig. 4B, Table S5), and the expression of these functionally relevant genes is similar in nuclei within the conserved clusters in all three species (Fig. 4C). This indicates that these 13 integrated clusters represent evolutionary conserved neuronal populations, constituting 57.6%, 61.7%, and 60.9% of neuronal nuclei in mice, baboons, and macaques, respectively.

Among the conserved integrated clusters, 11 were GABAergic. For example, integrated cluster 1 is conserved, consisting of nuclei with 38.3%, 39.8%, and 21.9% from mouse, baboon, and macaque, respectively. Mouse nuclei of this integrated cluster constitute 85.4% of the nuclei in mouse cluster DRD2_PDZD2 and 59.6% of the nuclei in mouse cluster PDE1C_CALCR. Baboon nuclei of this

integrated cluster constitute 89% of the nuclei in baboon cluster DRD2_PDZD2 and 97.7% of the nuclei in baboon cluster DRD2_GPC5. Macaque nuclei of this integrated cluster constitute 86.7% of the nuclei in macaque cluster DRD2_PDZD2 (Table S5). These data suggest that integrated cluster 1 represents a conserved neuronal population across three species and that the neuronal clusters, DRD2_PDZD2 and PDE1C_CALCR in mouse, DRD2_PDZD2 and DRD2_GPC5 in baboon, and DRD2_PDZD2 in macaque, display high transcriptional correspondence. Nuclei of integrated cluster 1 from different species exhibit conserved transcriptional profile of their marker gene expression (Fig. S6D) as well as functionally relevant gene panels (Fig. 4C).

The harmonization also revealed two conserved clusters of glutamatergic neurons. In the conserved integrated cluster 9, the mouse cluster SLC17A6_TCF7L2 exhibited high transcriptional correspondence to SLC17A6_SCL17A7 in baboon and SLC17A6_CCK in macaque. Integrated cluster 20 represented a conserved cholinergic (also glutamatergic based on the expression of *Slc17a8*/*SLC17A8*) neuronal population. Mouse cholinergic neurons formed a single cluster, CHAT_SLC5A7, and 73.2% of the nuclei from this mouse cholinergic cluster exhibited high transcriptional correspondence with the CHAT_MCC clusters in NHPs.

<u>Divergent ventral pallidum neuronal populations</u>

Despite being largely conserved, VP neurons also exhibit several species-specific characteristics. We identified 10 integrated clusters that were not conserved across all three species (Integrated clusters 3, 8, 13, 17, 18, 19, 22, 23, 24, 25, Fig 4B). Among these, three integrated clusters are conserved only between primates with no homologue in rodents (Integrated clusters 18, 19 and 23). One such cluster (Integrated cluster 18) was marked by expression of *DRD2* and *PMEPA1*. *PMEPA1* is an androgen responsive gene that has been characterized for its essential and reciprocal regulation of androgen receptor (AR) signaling (*45*). Additional genes that differentiated the DRD2_PMEMPA1 cluster with other neuronal clusters in both NHP species included *ACVR1*, *SORCS3, FOXN3, FGF13,* and *MOXD1*, which are critical for axonal remodeling and synaptic regulation (Fig. S6E). This raises the possibility that this NHP conserved cluster represents a unique transcriptional cell state reflecting the increased neuronal plasticity of NHPs.

While some glutamatergic neuronal clusters are transcriptionally conserved as described above, glutamatergic neurons overall represented a higher proportion of VP neurons in mice (9.9% of mouse neuronal nuclei, Fig 1E), relative to either primate species (2.7% of baboon neuronal nuclei and 6.6% of macaque neuronal nuclei, Fig 3D,G). In addition, some glutamatergic populations exhibiting divergence across species. The minor glutamatergic clusters in mouse, SLC17A6_MASP1 (integrated cluster 22) and SLC17A7_CCK (integrated cluster 24), had no transcriptional homologue in primate species, suggesting these clusters diverge between mouse and NHP.

Finally, we identified a second distinct cholinergic cluster (integrated cluster 23), corresponding to CHAT_VIPR2 in both macaques and baboons. This NHP neuronal population corresponds less strongly to the mouse cholinergic neurons compared to the conserved CHAT_MCC population. The NHP CHAT_VIPR2 cluster is marked by expression of the vasopressin receptor *VIPR2*, raising the possibility that these populations are differently subjected to excitation by vasopressin from exogenous sources or by local release from VP neurons (Fig. S6F). *Vipr2* is not significantly expressed in mouse cholinergic neurons.

Discussion

The basal ganglia are highly conserved throughout vertebrates, and our results underscore this conservation of the VP across rodents and primates at the transcriptional level. The VP is classically considered a GABAergic nucleus with cholinergic neurons which comprise part of the basal forebrain cholinergic system (*14*, *46*–*52*) while more contemporary work has identified that glutamatergic neurons comprise a distinct subpopulation (*6*, *7*). Our results confirm that the division of VP neurons into these broader neurochemical classes is valid and holds across mammalian species. Each of these neurochemical classes is comprised of distinct transcriptional subtypes, which are also largely conserved

across mammalian species. Intriguingly, the proportion of neurons represented in each of these subclasses diverged between species; while putative GABAergic neurons comprised the majority of VP neurons in all species, primates exhibited a smaller proportion of glutamatergic neurons and a larger proportion of cholinergic cells relative to mice. VP cholinergic neurons project to either the frontal cortex or amygdala (*53*), future work will establish whether the two distinct cholinergic clusters in NHPs map onto these projection targets. Alternatively, since only one cholinergic cluster had a homologous cluster in mice, our results could indicate evolutionary drift in the neuronal subtypes essential for the specialized functional role in the NHP. This diversification in the NHP cell types could also be a product of the VP expansion or possible integration of new sensory signals in the VP (*54*–*62*).

We identified 20 neuronal subtypes in mouse VP, marked by enrichment of neuropeptides, neurotransmitter receptors, and transcription factors. While foundational work has leveraged Cre driver lines (i.e. *Slc32a1*, *Slc17a6*, *Pvalb*, *Drd3*) to dissect VP circuit function, our results argue that these strategies do not correspond to molecularly defined VP subtypes. One framework for interpreting the heterogeneity of the VP is that VP cell types represent a combination of neurons from adjacent structures, including the ventral striatum and extended amygdala (*63*). Our results corroborate this interpretation at the transcriptional level. Specifically, we identified VP populations in mice that share marker genes for accumbal medium sized spiny neurons (*PDZD2* colocalized with either the *DRD1* or *DRD2* (*30*, *31*, *64*), clusters with transcriptional homologues in the extended amygdala (SLC17A7_CCK, DNAH5_VIPR2; *28*, *65*, *66*) and glutamatergic neurons with transcriptional homology to those expressed in BNST (SLC17A6_MASP1; *26*, *30*, *31*). Recent reports have corroborated this interpretation, finding that transcriptionally defined cell types are expressed in multiple forebrain structures that share borders with the VP (26, 33, 34). However, it is critical to note that while AIBS MERFISH data was generated using a 500-gene panel covering unique sets of marker genes across the brain, these marker genes are not fine-tuned to label molecularly defined transcriptomic clusters unique to several brain regions. Therefore, the spatial identity of identified transcriptional profiles of the VP neurons may not be detected with these approaches.

Spatial validation revealed a lack of topographical organization of neuronal populations marked by GABA, glutamate and acetylcholine, with a lack of discrete boundaries between cell types nor continuous gradients of gene expression. However, we uncovered distinct spatial organization of the specific sub clusters of GABAergic and glutamatergic clusters. Prior pharmacology and functional studies have demonstrated functional anatomical subdivisions of VP. For example, infusion of opioids into the posterior VP enhances hedonic reactions to palatable stimuli, while infusion into the anterior VP suppresses these same reactions, and GABA-mediated inactivation of the VP promoted feeding, with effects more pronounced in medial VP (*67*). Our results suggest that differences in topography transcriptionally-defined cell types across the anterior-posterior gradient within the VP may contribute to these functional differences.

The VP is composed of non-overlapping populations of anatomically-defined projection neurons to the nucleus accumbens, lateral habenula, thalamus, cortex, and midbrain which have been causally linked to distinct dimensions of reward processing (*9*, *68*–*73*). It will be critical to know the anatomical identity of these transcriptionally-defined populations to understand how these cell types modulate behavior. Moreover, transcriptomes are not static, responding to the local environment even in terminally differentiated, post-mitotic neurons. Given interest in the VP as a target for depression (*9*, *74*), obesity (*11*, *75*) and substance use disorders (*2*, *76*, *77*), future work necessitates understanding how experience and environmental stressors alter the transcriptional profile of these VP cell types, and ultimately how these transcriptional changes alter neuronal and circuit function.

Methods

Subjects

Mouse. C57Bl6J mice (aged 10-15 weeks) were used for snRNA-sequencing (n=10 males, 10 females), in situ hybridization (1M, 2F), and immunohistochemistry (2M, 2F) experiments. Mice were housed in groups of 2-5 with ad libitum access to standard rodent lab chow and water, on a 12h light cycle (light onset 7 am, offset 7 pm). All procedures were approved by the institutional animal care and use committee at Washington University School of Medicine (WashU).

Primates. 2 male olive baboons (3.62 and 4.32 years old), 1 male rhesus macaque (10.7 years old), and 3 female rhesus macaques (5.87, 6.66, and 17.67 years old). All animals were pair housed on a 12-hour on/12-hour off lighting schedule with ad libitum access to food and water. Animals were fed standard primate chow twice daily and provided fruit and vegetable enrichment daily. Macaques were observed by trained veterinary technicians daily in their home cages. The Institutional Animal Care and Use Committee and the Institutional Biosafety Committee at the ONPRC and Oregon Health and Science University (OHSU) approved all experimental procedures. All of the guidelines specified in the National Institutes of Health Guide for the Care and Use of Laboratory Animals (National Research Council, 2011) were strictly followed.

Mouse Tissue Collection for RNA-seq

To collect mouse VP tissues for sequencing, animals were anesthetized with ketamine cocktail, and perfused with ice-cold NMDG-based cutting solution (NMDG 93 mM, KCl 2.5 mM, NaH_2PO_4 1.25 mM, $NaHCO_3$ 30 mM, HEPES 20 mM, Glucose 25 mM, Ascorbic acid 5 mM, Tiourea 2 mM, Sodium Pyruvate 3 mM, $MgSO_4$ 10 mM, $CaCl_2$ 0.5 mM, N-acetylcysteine 12 mM; pH adjusted to 7.3 with 12N HCl, and bubbled with 95% O_2 and 5% CO_2). Brain was dissected submerged in ice-cold NMDG-based cutting solution and sliced coronally into sections with 400 µm thickness using a Compresstome (Precisionary, VF-210-0Z). VP regions were micro-dissected under a microscope (Leica S9i) in a sterile petri dish treated with RNAse-X on dry ice, using a reusable 0.75 mm biopsy punch (WPI 504638). For each sequencing sample, tissues from five mice were pooled and collected into a nucleus-free centrifuge tube placed on dry ice. Samples were stored at -80℃ before nuclei isolation.

Primate Tissue Collection for RNA-seq

Freshly-dissected, unfixed, and flash-frozen VP tissue punches were acquired from two non-human primate species. Necropsies and tissue collections were performed as previously described(*78–80*). Animals were sedated with ketamine (10 mg/kg) and then deeply anesthetized with sodium pentobarbital followed by exsanguination. The brain and spinal cord were perfused through the ascending carotid artery with 1 L of 0.9% ice-cold saline. The brain was then removed from the skull (< 30 minutes post-mortem), deposited into an ice-cold bath of saline for transport, and placed into an ice-cold, steel brain matrix (Electron Microscopy Sciences). A custom 3D printed brain matrix was used to section the baboon brains. Each brain was positioned in the brain matrix with the ventral surface facing up. The anterior medial temporal sulcus, posterior to the temporal pole, and anterior to the rhinal sulcus was identified on the ventral surface of the temporal lobe. A carbon steel knife blade (Thomas Scientific) was inserted into the slot in brain matrix that was most closely aligned and orthogonal to the beginning of the anterior medial temporal sulcus. Additional knife blades were inserted anterior and posterior to the first knife blade inserted in 2 mm increments. The resulting 2 mm bilateral brain slabs were then removed from the brain matrix and laid out flat in sterile petri dishes treated with RNase-X and stored at -80°C. The petri dishes rested on an aluminum plate secured to a chamber filled with dry ice. The plate temperature was maintained at -30°C to -15°C for up to two hours while tissue punches were acquired and flash frozen.

Brain slabs in which the VP was clearly visible below the anterior commissure on both sides of the slab were identified and 1.0-2.5 mm in diameter tissue punches (1-3 per site) were taken through the full width of the slab. Tissue punches were checked to ensure they did not contain white matter and then inserted into DNase- and RNase-free 1.5 mL microcentrifuge tubes that were inserted into powderized dry ice.

405 Ethanol was poured onto the dry ice to flash freeze the tissue punches. All tissue punches were acquired
406 within 90 minutes postmortem. The punched brain slabs were then post fixed in 4% paraformaldehyde
407 for 48 hours, cryoprotected in 30% sucrose, and then sectioned in 40 μm sections for histological
408 analyses.

409 Single-nuclei isolation

410 Nuclear extraction for both mice and primates was performed with density gradient centrifugation
411 according to the protocol described previously with minor modifications (*81*). Samples were moved from
412 -80℃ and thawed on ice for 2 minutes. Tissues were transferred to a dounce homogenizer in
413 homogenization buffer (0.25 M sucrose, 25 mM KCl, 5 mM $MgCl_2$, 10 mM Tris-HCl, pH 8.0, 5 μg/mL
414 actinomycin, 1% BSA, and 0.08 U/μl RNase inhibitor, 0.01% NP40) on ice. Samples were homogenized
415 for 10 strokes with the loose pestle in a total volume of 1 mL, followed by 10 additional strokes with the
416 tight pestle. The tissue homogenate was then passed through a 50 μm filter and diluted 1:1 with working
417 solution (50% iodixanol, 25 mM KCl, 5 mM $MgCl_2$, and 10 mM Tris-HCl, pH 8.0). Nuclei were layered
418 onto an iodixanol gradient after homogenization and ultracentrifuged as described previously. After
419 ultracentrifugation, nuclei were collected between the 30 and 40% iodixanol layers and diluted with
420 resuspension buffer (1xPBS with 1% BSA, and 0.08 U/μl RNase inhibitor). Nuclei were centrifuged at
421 500 g for 10 min at 4°C and resuspended in resuspension buffer with 5 ng/μl of 7-AAD. FACS was carried
422 out to further remove cellular debris. 7-AAD+ events were collected using a 100 μm nozzle on a BD
423 FACSAria III instrument into a 1.5 mL microcentrifuge tube. Nuclei in the post-FACS samples were
424 counted using a hemocytometer and diluted to around 400 nuclei/μl.

425 snRNA-seq

426 Nuclei were processed and sequenced according to the manufacturer's manual of 10X Genomics
427 Chromium Single Cell Gene Expression 3' V3.1 Assay. Libraries were sequenced on a NovaSeq6000
428 with 150 cycles each for Read1 and Read2, targeting 50,000 paired reads/nucleus. Raw sequencing data
429 from individual libraries were processed and mapped to the reference genome and the gene-cell counts
430 matrices from all snRNA-seq libraries of the same species were concatenated using 10X Genomics
431 cellranger-6.1.2.

432 *Quality control and clustering of snRNA-seq.* The analysis was carried out using R package Seurat
433 (V4.3.0) (*82*) with data derived from different species analyzed separately. Nuclei with at least 500 unique
434 genes, less than 15,000 unique transcript counts, and fewer than 2% for mouse and 5% for baboon and
435 macaque of the counts from mitochondrial genes were included in the analysis. Raw counts were scaled
436 to 10,000 transcripts per nucleus using NormalizeData() function to control the sequencing depth
437 between nuclei. Counts were centered and scaled for each gene using ScaleData() function. Highly
438 variable genes were identified using FindVariableFeatures() and the top 20 principal components (PCs)
439 were retrieved with RunPCA() using default parameters. For dimension reduction and visualization,
440 Uniform Manifold Approximation and Projection (UMAP) coordinates were calculated based on the top
441 20 PCs using RunUMAP(). Nuclei clustering was performed using FindClusters() based on the variable
442 features from the top 20 principal components, with resolution at 0.6, and the marker genes for each
443 cluster were identified using FindAllMarkers() comparing nuclei in one cluster to all other nuclei. Clusters
444 enriched of low-quality nuclei or doublets were identified if they meet any of the following criteria: 1).
445 Assigned to a cluster with no significantly enriched marker genes (FDR < 0.05, log2FC > 1); 2). Assigned
446 to a cluster in which five or more mitochondrial genes were identified among the top 20 marker genes
447 (sorted by avg_log2FC). The remaining clusters were either assigned as neuronal if they expressed high
448 level of neuronal marker genes (*Rbfox3*, *Snap25*, and *Syt1*), or as non-neuronal if they exhibited high
449 expression level of any of the non-neuronal marker genes (*Sparc*, *Mbp*, or *Apoe*). Nuclei from neuronal
450 clusters and non-neuronal clusters were sub-clustered separately, and the clusters enriched with low-
451 quality nuclei or doublets were identified again as described previously.

452 *Mouse libraries*. For the mouse dataset, five libraries from four samples generated a total of 44,518 nuclei
453 that passed initial quality control cutoffs. Among them, 6,388 nuclei were identified as doublets or low-

quality and thus excluded from the dataset, yielding a final dataset containing 38,130 nuclei (24,870 neuronal nuclei and 13,260 non-neuronal nuclei).

Baboon libraries. For the baboon dataset, six libraries were generated from four biological samples of two individual animals, generating a total of 60,209 nuclei that passed initial quality control cutoffs. Among them, 2,485 nuclei were identified as doublets or low-quality and thus excluded from the dataset, yielding a final dataset containing 57,724 nuclei (16,293 neuronal nuclei and 41,431 non-neuronal nuclei). While baboon nuclei from individual libraries clustered together on the UMAP indicating a low batch effect across libraries (Fig. S5C), snRNA-seq libraries of one animal identified much fewer neuronal nuclei compared to those of another animal (5.6 ± 0.8% compared to 36.1 ± 11.8%, mean ± standard deviation, Fig. S5E). This difference in neuronal nuclei enrichment was likely due to variations from individual animals (e.g. age or other individual factors) and/or tissue procurement process.

Macaque libraries. For the macaque dataset, six libraries were generated from four biological samples of three individual animals, generating a total of 49,802 nuclei that passed initial quality control cutoffs. During the initial clustering, individual macaque snRNA-seq libraries showed similar cell type compositions (Fig. S5F) and clustered together on the UMAP space (Fig. S5D), with the exception that one snRNA-seq library exhibited mild transcriptional variation compared to other libraries (Fig. S5D, Table S4). This altered gene expression to this library, likely due to technical variation in the tissue extraction and procurement process. To correct for the batch effect, the gene expression matrices from individual libraries were normalized using FindIntegrationAnchors() and integrated using IntegrateData(), both with the normalization method set as 'SCT'. Clustering was carried out as described above. Among them, 260 nuclei were identified as doublets or low-quality and thus excluded from the dataset, yielding a final dataset containing 49,542 nuclei (13,696 neuronal nuclei and 35,846 non-neuronal nuclei).

Cluster Annotation

Clusters were annotated and named based on the expression of canonical markers for each cell type: neurons (*Rbfox3, Snap25, Syt1* mouse; *RBFOX3, SNAP25, SYT1* primate), astrocytes (*Aldoc*, *Aqp4*, *Slc1a2* mouse; *ALDOC*, *AQP4*, *SLC1A2* primate), choroid epithelial cells (*Ttr*, *Folr1*, *Clic6* mouse; *TTR*, *FOLR1*, *CLIC6* primate), macrophages (*Pf4, Cd74, Mrc1* mouse; *PF4, CD74, MRC1* primate), microglial cells (*Tmem119, Cx3cr1, Hexb* mouse; *TMEM119, CX3CR1, HEXB* primate), oligodendrocytes (*Mbp, Plp1, Cnp* mouse; *MBP, PLP1, CNP primate*), OPC (*Pdgfra, Olig1, Olig2* mouse; *PDGFRA, OLIG1, OLIG2* primate), and vascular cells (*Dcn, Mgp, Cped1* mouse, *DCN, MGP, CPED1* primate). To identify neuronal cell types, nuclei in the neuronal clusters were extracted to be re-clustered. Initial independent clustering of each species resulted in 20 clusters in mice, 20 clusters in baboon, and 24 clusters in macaque. Each cluster was assigned a neurochemical identity based on the expression of canonical marker genes for glutamatergic, GABAergic, and cholinergic populations: Vesicular glutamate transporter 1 and 2, (*Slc17a6*, *Slc17a7* mouse; *SLC17A6*, *SLC17A7* primate), glutamic acid decarboxylase; vesicular gaba transporter (*Gad2*, *Slc32a1* mouse, *GAD2*, *SLC32A1* primate), or choline acetyltransferase, high-affinity choline transporter (*Chat*, *Slc5a7* mouse; *CHAT*, *SLC5A7* primate). Clusters were further annotated and named based on differentially expressed marker genes conserved across species. Mouse cluster names are presented in uppercase to be consistent with primate names.

Cross-Species Analysis

To harmonize VP neurons across species, neuronal nuclei from each species were selected. Gene names in the mouse dataset were converted to primate genes using biomaRt package (*83*, *84*). Baboon, macaque, and mouse datasets were jointly clustered using Seurat V4 as described above (Fig. S4A). To facilitate accurate comparative analysis across species, nuclei of different species were integrated (Fig. 4A). Top 1000 variable genes in each species were used to generate an integrative expression matrix, and integration anchors were identified by running FindIntegrationAnchors(). Data of different species were then integrated using IntegrateData(). The top 20 PCs were used for clustering and UMAP visualization. To establish correspondence between cross-species integrated clusters and mouse, macaque, and baboon clusters (Fig. 4B), which were generated independently by the clustering approach described above, we calculated the fraction of nuclei in each neuronal cluster defined by independent

analysis for each species that mapped to each integrated cluster. Integrated clusters consisting of nuclei that made up over 40% of the nuclei from at least one neuronal cluster per species are considered conserved clusters. Cutoff nuclei from each species >30. That leaves cluster 17 absent of baboon, cluster 25 absent of baboon, and cluster 26 absent of mouse and baboon. All other integrated clusters are identified as species-specific. To assess the transcriptional similarity of cell types across different species (Fig. S4D), expression values of conserved marker genes (Log2FC>0.5, FDR<0.05 in all species) in all nuclei of each neuronal cluster identified by independent analyses were averaged for each gene using AverageExpression() and then pairwise Pearson's correlation coefficient between all pairs of clusters in each dataset was computed.

Gene Ontology (GO) Analysis

GO analysis was performed using topGO (version: 2.40.0) in R. Conserved marker genes (log2FC > 0.5, FDR < 0.01 in all examined species) were used as the input gene list. For comparison, the background gene list included all genes with average expression > 0.5 in the respective nuclei being analyzed. Genes were annotated for their biological process and associated gene ontology terms. Enrichment is defined as the number of annotated genes observed in the input list divided by the number of annotated genes expected from the background list. GO terms with at least 10 annotated genes and enrichment p-value < 0.05 were returned except otherwise specified.

Hiplex Fluorescent In Situ Hybridization (HiPlex FISH)

Sample preparation. Mice were anesthetized with isoflurane, sacrificed, and brains were rapidly dissected then flash frozen in isopentane at -80°C. Flash-frozen brains were hemisected and sectioned at a thickness of 14um on a cryostat (Leica CM1850; Leica Biosystems, Deer Park, USA). Sections spanning the rostrocaudal extent of the VP were collected on Superfrost Plus microscope slides (Fisher Scientific, Pittsburgh, USA). Slides were stored at -80°C until further use. Probes for *Gad2, Drd1, Drd2, Drd3, Sst, Tac1, Chat, CCK, Slc17a6, and Trp73* mRNA were hybridized and fluorescently labeled using the RNAScope HiPlex12 Reagent Kit v2 (488, 550,650) Assay (Advanced Cell Diagnostics, Newark, USA) according to manufacturer's instructions. DAPI was used as a counterstain and slides were coverslipped using Gold Prolong antifade mounting medium (Invitrogen, Eugene, OR)

Signal detection and analysis. Tilescans and z-stacks encompassing the entire VP were acquired using a confocal microscope (Leica Stellaris 5 LIA; Leica Microsystems, Deer Park, USA) under the 20X objective. Channels collected across rounds of imaging were aligned in ACDBio HiPlex Registration software using the DAPI signal. Tiff files were then analyzed in QuPath (v0.5.1). The signal for each channel was detected using the 'analyze object' function, threshold detection level, sigma parameter, and minimum area were determined for each probe and settings were held consistent across sections. Colocalization was defined as centroids within 4um, colocalized with a DAPI-positive nucleus. Cluster membership for each nucleus was assigned based on combinatorial co-expression of probes. Nuclear coordinates were then aligned to the anatomical landmarks of the VP according to the atlas of Paxinos and Watson (*85* ; Python v. 3.12).

Immunohistochemistry

Sample preparation. Mice were anesthetized with isoflurane, PFA-perfused, and sacrificed. Brains were dissected and stored in 30% sucrose cryoprotectant at 4°C until brains were fully submerged. 30 µm sections through the rostrocaudal extent of the VP were collected using a cryostat (Leica CM1850; Leica Biosystems, Deer Park, USA) and then hemisected. The sections were placed in blocking solution (94.5% PBS, 5% Normal Donkey Serum, 0.1% Triton X) for one hour. Primary antibodies were allowed to incubate on an orbital shaker overnight at 4°C. Antibodies were diluted with blocking solution at the following concentrations: NeuN (ABN90, Sigma-Aldrich) 1:3000, Iba1 (234 009, Synaptic Systems Company) 1:1000, Sox9 (ab185966, Abcam) 1:500. Following primary antibody incubation, we performed three 10-minute washes in PBS, using fresh PBS for each wash. The following secondary antibodies were then applied and incubated for 2 hours at room temperature on an orbital shaker: Goat anti-guinea pig Alexa Fluor 647 (A-21450, ThermoFisher) 1:1000, goat-anti-chicken Alexa Fluor 488 (A-11039,

ThermoFisher) 1:1000, donkey anti-rabbit Alexa Fluor 594 (A-21207, ThermoFisher) 1:1000. Sections were then mounted onto Superfrost Plus microscope slides (Fisher Scientific, Pittsburgh, USA) and coverslipped using Fluoromount-G, with DAPI (Invitrogen, USA).

Image acquisition and analysis. Images along the anterior-posterior extent of the VP were imaged on a Zeiss AxioImager.Z2 (Apotome) at 20x. ROIs were captured as 600,000 µM ^3 (50000µM ^ 2, 12 µM z-stacks) for quantification of NeuN, Iba1, and Sox9. Supervised pixel and object classification was performed using Ilastik machine-learning software (v1.4, *86*). Pixel classification was done by drawing annotative lines on cells, across the diameter of the cells, and on the background. After thresholding and filtering (hysteresis thresholding for NeuN and simple thresholding for Iba1 and Sox9), extracted objects were annotated as cells or backgrounds. We validated the Ilastik model by randomly selecting 10 ROIs and corroborating counts generated manually and in Ilastik. Images were then batch processed using the pixel and object classification models before exporting counts for NeuN (neurons), Iba1 (microglia), and Sox9 (astrocytes).

Data availability

Raw and processed data of snRNA-seq experiments included in this study are in the process of being deposited to the NCBI Gene Expression (GEO). Processed snRNA-seq data included in this study are available via Washington University Digital Commons Data@Becker with DOI: 10.17632/fyz3cn8r32.1.

Acknowledgments

This work was funded by National Institute on Drug Abuse: R01DA056829 (V.K.S and M.C.C), R01DA049924, R01DA058755 (M.C.C), National Institute of Diabetes and Digestive and Kidney Diseases: R01DK128475, K01DK115634 (V.K.S), and by the DRC at Washington University NIH P30DK020579 (M.C.C). M.R.L is part of the NINDS Neuroscience Postbaccalaureate Program at Washington University, which is supported by National Institute of Neurological Disorders and Stroke: R25NS130965-02. We thank Flow Cytometry & Fluorescence Activated Cell Sorting Core in the Department of Pathology and Immunology at Washington University School of Medicine for help with FACS. We thank the Genome Technology Access Center at McDonnell Genome Institute at Washington University School of Medicine for help with snRNA-seq library construction and sequencing. The Center is partially supported by NCI Cancer Center Support Grant #P30 CA91842 to the Siteman Cancer Center from the National Center for Research Resources (NCRR), a component of the National Institutes of Health (NIH), and NIH Roadmap for Medical Research. We would like to thank the Papouin lab at Washington University for use of the NeuN, Iba1, and Sox9 antibodies. We are grateful to members of the Creed and Samineni labs for their helpful discussion of the manuscript and experimental design.

Author contributions

V.K.S., M.C.C, and L.Y. conceptualized the project and designed the experiments; L.Y.H.H, Y.Z, and M.R.H performed the library preparation. L.Z.F, M.R.L, and C.S.X performed HiPlex FISH, immunohistochemistry, and analyzed the data; L.Y. performed sequencing experiments and the sequencing analysis; V.C. performed NHP tissue dissections. L.Y., L.Z.F, V.C., V.K.S., and M.C.C wrote the manuscript with input from all authors.

Competing interest

The authors declare that they have no conflict of interest.

References

1. D. H. Root, R. I. Melendez, L. Zaborszky, T. C. Napier, The ventral pallidum: Subregion-specific functional anatomy and roles in motivated behaviors. *Prog Neurobiol* **130**, 29–70 (2015).

2. M. R. Farrell, Q. Ye, Y. Xie, J. S. D. Esteban, S. V. Mahler, Ventral pallidum GABA neurons bidirectionally control opioid relapse across rat behavioral models. *Addiction Neuroscience* **3**, 100026 (2022).

3. M. R. Farrell, J. S. D. Esteban, L. Faget, S. B. Floresco, T. S. Hnasko, S. V. Mahler, Ventral Pallidum GABA Neurons Mediate Motivation Underlying Risky Choice. *J. Neurosci.* **41**, 4500–4513 (2021).

4. J. A. Heinsbroek, A.-C. Bobadilla, E. Dereschewitz, A. Assali, R. M. Chalhoub, C. W. Cowan, P. W. Kalivas, Opposing Regulation of Cocaine Seeking by Glutamate and GABA Neurons in the Ventral Pallidum. *Cell Rep* **30**, 2018-2027.e3 (2020).

5. M. Stephenson-Jones, C. Bravo-Rivera, S. Ahrens, A. Furlan, X. Xiao, C. Fernandes-Henriques, B. Li, Opposing Contributions of GABAergic and Glutamatergic Ventral Pallidal Neurons to Motivational Behaviors. *Neuron* **105**, 921-933.e5 (2020).

6. L. Faget, V. Zell, E. Souter, A. McPherson, R. Ressler, N. Gutierrez-Reed, J. H. Yoo, D. Dulcis, T. S. Hnasko, Opponent control of behavioral reinforcement by inhibitory and excitatory projections from the ventral pallidum. *Nat Commun* **9**, 849 (2018).

7. J. Tooley, L. Marconi, J. B. Alipio, B. Matikainen-Ankney, P. Georgiou, A. V. Kravitz, M. C. Creed, Glutamatergic Ventral Pallidal Neurons Modulate Activity of the Habenula–Tegmental Circuitry and Constrain Reward Seeking. *Biological Psychiatry* **83**, 1012–1023 (2018).

8. M. Moaddab, M. H. Ray, M. A. McDannald, Ventral pallidum neurons dynamically signal relative threat. *Commun Biol* **4**, 43 (2021).

9. D. Knowland, V. Lilascharoen, C. P. Pacia, S. Shin, E. H.-J. Wang, B. K. Lim, Distinct Ventral Pallidal Neural Populations Mediate Separate Symptoms of Depression. *Cell* **170**, 284-297.e18 (2017).

10. K. S. Smith, K. C. Berridge, The Ventral Pallidum and Hedonic Reward: Neurochemical Maps of Sucrose “Liking” and Food Intake. *J. Neurosci.* **25**, 8637–8649 (2005).

11. S. Gendelis, D. Inbar, K. Inbar, S. Mesner, Y. M. Kupchik, Metaplasticity in the Ventral Pallidum as a Potential Marker for the Propensity to Gain Weight in Chronic High-Calorie Diet. *J. Neurosci.* **40**, 9725–9735 (2020).

12. A. R. Childress, R. N. Ehrman, Z. Wang, Y. Li, N. Sciortino, J. Hakun, W. Jens, J. Suh, J. Listerud, K. Marquez, T. Franklin, D. Langleben, J. Detre, C. P. O’Brien, Prelude to Passion: Limbic Activation by “Unseen” Drug and Sexual Cues. *PLoS ONE* **3**, e1506 (2008).

13. W. K. Simmons, K. M. Rapuano, J. E. Ingeholm, J. Avery, S. Kallman, K. D. Hall, A. Martin, The ventral pallidum and orbitofrontal cortex support food pleasantness inferences. *Brain Struct Funct* **219**, 473–483 (2014).

14. L. Heimer, R. D. Wilson, “Golgi Centennial Symposium. Proceedings. Edited by M. Santini. Raven Press, New York© 1975.” (Raven Press (ID), 1975), p. 177.

15. H. Pribiag, S. Shin, E. H.-J. Wang, F. Sun, P. Datta, A. Okamoto, H. Guss, A. Jain, X.-Y. Wang, B. De Freitas, P. Honma, S. Pate, V. Lilascharoen, Y. Li, B. K. Lim, Ventral pallidum DRD3

potentiates a pallido-habenular circuit driving accumbal dopamine release and cocaine seeking. *Neuron* **109**, 2165-2182.e10 (2021).

16. G. Morais-Silva, R. R. Campbell, H. Nam, M. Basu, M. Pagliusi, M. E. Fox, C. S. Chan, S. D. Iñiguez, S. Ament, N. Cramer, M. T. Marin, M. K. Lobo, Molecular, Circuit, and Stress Response Characterization of Ventral Pallidum Npas1-Neurons. *J. Neurosci.* **43**, 405–418 (2023).

17. D. J. Ottenheimer, B. A. Bari, E. Sutlief, K. M. Fraser, T. H. Kim, J. M. Richard, J. Y. Cohen, P. H. Janak, A quantitative reward prediction error signal in the ventral pallidum. *Nat Neurosci* **23**, 1267–1276 (2020).

18. D. J. Ottenheimer, K. Wang, X. Tong, K. M. Fraser, J. M. Richard, P. H. Janak, Reward activity in ventral pallidum tracks satiety-sensitive preference and drives choice behavior. *Sci. Adv.* **6**, eabc9321 (2020).

19. J. M. Richard, F. Ambroggi, P. H. Janak, H. L. Fields, Ventral Pallidum Neurons Encode Incentive Value and Promote Cue-Elicited Instrumental Actions. *Neuron* **90**, 1165–1173 (2016).

20. D. H. Root, D. J. Barker, S. Ma, K. R. Coffey, A. T. Fabbricatore, M. O. West, Evidence for learned skill during cocaine self-administration in rats. *Psychopharmacology* **217**, 91–100 (2011).

21. A. J. Tindell, K. S. Smith, S. Peciña, K. C. Berridge, J. W. Aldridge, Ventral Pallidum Firing Codes Hedonic Reward: When a Bad Taste Turns Good. *Journal of Neurophysiology* **96**, 2399–2409 (2006).

22. A. Fujimoto, Y. Hori, Y. Nagai, E. Kikuchi, K. Oyama, T. Suhara, T. Minamimoto, Signaling Incentive and Drive in the Primate Ventral Pallidum for Motivational Control of Goal-Directed Action. *J Neurosci* **39**, 1793–1804 (2019).

23. N. M. Ledbetter, C. D. Chen, I. E. Monosov, Multiple Mechanisms for Processing Reward Uncertainty in the Primate Basal Forebrain. *J Neurosci* **36**, 7852–7864 (2016).

24. Y. Tachibana, O. Hikosaka, The primate ventral pallidum encodes expected reward value and regulates motor action. *Neuron* **76**, 826–837 (2012).

25. S. J. Mitchell, R. T. Richardson, F. H. Baker, M. R. DeLong, The primate globus pallidus: neuronal activity related to direction of movement. *Exp Brain Res* **68**, 491–505 (1987).

26. D. J. Ottenheimer, R. C. Simon, C. T. Burke, A. J. Bowen, S. M. Ferguson, G. D. Stuber, Single-cell sequencing of rodent ventral pallidum reveals diverse neuronal subtypes with non-canonical interregional continuity. [Preprint] (2024). https://doi.org/10.1101/2024.03.18.585611.

27. C. Ortiz, J. F. Navarro, A. Jurek, A. Märtin, J. Lundeberg, K. Meletis, Molecular atlas of the adult mouse brain. *Sci. Adv.* **6**, eabb3446 (2020).

28. Z. Yao, C. T. J. Van Velthoven, M. Kunst, M. Zhang, D. McMillen, C. Lee, W. Jung, J. Goldy, A. Abdelhak, M. Aitken, K. Baker, P. Baker, E. Barkan, D. Bertagnolli, A. Bhandiwad, C. Bielstein, P. Bishwakarma, J. Campos, D. Carey, T. Casper, A. B. Chakka, R. Chakrabarty, S. Chavan, M. Chen, M. Clark, J. Close, K. Crichton, S. Daniel, P. DiValentin, T. Dolbeare, L. Ellingwood, E. Fiabane, T. Fliss, J. Gee, J. Gerstenberger, A. Glandon, J. Gloe, J. Gould, J. Gray, N. Guilford, J. Guzman, D. Hirschstein, W. Ho, M. Hooper, M. Huang, M. Hupp, K. Jin, M. Kroll, K. Lathia, A. Leon, S. Li, B. Long, Z. Madigan, J. Malloy, J. Malone, Z. Maltzer, N. Martin, R. McCue, R. McGinty, N. Mei, J. Melchor, E. Meyerdierks, T. Mollenkopf, S. Moonsman, T. N. Nguyen, S. Otto, T. Pham, C. Rimorin, A. Ruiz, R. Sanchez, L. Sawyer, N. Shapovalova, N. Shepard, C. Slaughterbeck, J. Sulc, M. Tieu, A. Torkelson, H. Tung, N. Valera Cuevas, S. Vance, K. Wadhwani, K. Ward, B. Levi, C. Farrell, R. Young, B. Staats, M.-Q. M. Wang, C. L. Thompson, S. Mufti, C. M. Pagan, L. Kruse, N. Dee, S. M. Sunkin, L. Esposito, M. J. Hawrylycz, J. Waters, L. Ng, K. Smith,

680 B. Tasic, X. Zhuang, H. Zeng, A high-resolution transcriptomic and spatial atlas of cell types in the
681 whole mouse brain. *Nature* **624**, 317–332 (2023).

682 29. Allen Institute, H. Zeng, Mouse whole-brain transcriptomic cell type atlas - MERSCOPE v1. [
683 Collection / Dataset]. Brain Image Library. https://doi.org/10.35077/g.610, (2023).

684 30. E. S. Lein, M. J. Hawrylycz, N. Ao, M. Ayres, A. Bensinger, A. Bernard, A. F. Boe, M. S. Boguski,
685 K. S. Brockway, E. J. Byrnes, L. Chen, L. Chen, T.-M. Chen, M. Chi Chin, J. Chong, B. E. Crook,
686 A. Czaplinska, C. N. Dang, S. Datta, N. R. Dee, A. L. Desaki, T. Desta, E. Diep, T. A. Dolbeare, M.
687 J. Donelan, H.-W. Dong, J. G. Dougherty, B. J. Duncan, A. J. Ebbert, G. Eichele, L. K. Estin, C.
688 Faber, B. A. Facer, R. Fields, S. R. Fischer, T. P. Fliss, C. Frensley, S. N. Gates, K. J. Glattfelder,
689 K. R. Halverson, M. R. Hart, J. G. Hohmann, M. P. Howell, D. P. Jeung, R. A. Johnson, P. T. Karr,
690 R. Kawal, J. M. Kidney, R. H. Knapik, C. L. Kuan, J. H. Lake, A. R. Laramee, K. D. Larsen, C. Lau,
691 T. A. Lemon, A. J. Liang, Y. Liu, L. T. Luong, J. Michaels, J. J. Morgan, R. J. Morgan, M. T.
692 Mortrud, N. F. Mosqueda, L. L. Ng, R. Ng, G. J. Orta, C. C. Overly, T. H. Pak, S. E. Parry, S. D.
693 Pathak, O. C. Pearson, R. B. Puchalski, Z. L. Riley, H. R. Rockett, S. A. Rowland, J. J. Royall, M.
694 J. Ruiz, N. R. Sarno, K. Schaffnit, N. V. Shapovalova, T. Sivisay, C. R. Slaughterbeck, S. C. Smith,
695 K. A. Smith, B. I. Smith, A. J. Sodt, N. N. Stewart, K.-R. Stumpf, S. M. Sunkin, M. Sutram, A. Tam,
696 C. D. Teemer, C. Thaller, C. L. Thompson, L. R. Varnam, A. Visel, R. M. Whitlock, P. E.
697 Wohnoutka, C. K. Wolkey, V. Y. Wong, M. Wood, M. B. Yaylaoglu, R. C. Young, B. L. Youngstrom,
698 X. Feng Yuan, B. Zhang, T. A. Zwingman, A. R. Jones, Genome-wide atlas of gene expression in
699 the adult mouse brain. *Nature* **445**, 168–176 (2007).

700 31. Allen Institute for Brain Science, Allen Mouse Brain Atlas [dataset]. Available from mouse.brain-
701 map.org, (2004).

702 32. A. Nickerson Poulin, A. Guerci, S. El Mestikawy, K. Semba, Vesicular glutamate transporter 3
703 immunoreactivity is present in cholinergic basal forebrain neurons projecting to the basolateral
704 amygdala in rat. *J Comp Neurol* **498**, 690–711 (2006).

705 33. V. K. Samineni, J. G. Grajales-Reyes, G. E. Grajales-Reyes, E. Tycksen, B. A. Copits, C.
706 Pedersen, E. S. Ankudey, J. N. Sackey, S. B. Sewell, M. R. Bruchas, R. W. Gereau, Cellular,
707 circuit and transcriptional framework for modulation of itch in the central amygdala. *Elife* **10**,
708 e68130 (2021).

709 34. T. P. O'Leary, R. M. Kendrick, B. N. Bristow, K. E. Sullivan, L. Wang, J. Clements, A. L. Lemire, M.
710 S. Cembrowski, Neuronal cell types, projections, and spatial organization of the central amygdala.
711 *iScience* **25**, 105497 (2022).

712 35. M. Numan, M. J. Numan, N. Pliakou, D. S. Stolzenberg, O. J. Mullins, J. M. Murphy, C. D. Smith,
713 The effects of D1 or D2 dopamine receptor antagonism in the medial preoptic area, ventral
714 pallidum, or nucleus accumbens on the maternal retrieval response and other aspects of maternal
715 behavior in rats. *Behavioral Neuroscience* **119**, 1588–1604 (2005).

716 36. B. T. DiBenedictis, H. K. Cheung, E. R. Nussbaum, A. H. Veenema, Involvement of ventral pallidal
717 vasopressin in the sex-specific regulation of sociosexual motivation in rats.
718 *Psychoneuroendocrinology* **111**, 104462 (2020).

719 37. A. Westlind-Danielsson, E. Gould, B. S. McEwen, Thyroid Hormone Causes Sexually Distinct
720 Neurochemical and Morphological Alterations in Rat Septal-Diagonal Band Neurons. *Journal of*
721 *Neurochemistry* **56**, 119–128 (1991).

722 38. K. L. Chiou, X. Huang, M. O. Bohlen, S. Tremblay, A. R. DeCasien, D. R. O'Day, C. H. Spurrell, A.
723 A. Gogate, T. M. Zintel, Cayo Biobank Research Unit, M. G. Andrews, M. I. Martínez, L. M. Starita,
724 M. J. Montague, M. L. Platt, J. Shendure, N. Snyder-Mackler, A single-cell multi-omic atlas
725 spanning the adult rhesus macaque brain. *Sci. Adv.* **9**, eadh1914 (2023).

39. N. Micali, S. Ma, M. Li, S.-K. Kim, X. Mato-Blanco, S. K. Sindhu, J. I. Arellano, T. Gao, M. Shibata, K. T. Gobeske, A. Duque, G. Santpere, N. Sestan, P. Rakic, Molecular programs of regional specification and neural stem cell fate progression in macaque telencephalon. *Science* **382**, eadf3786 (2023).

40. E. Sjöstedt, W. Zhong, L. Fagerberg, M. Karlsson, N. Mitsios, C. Adori, P. Oksvold, F. Edfors, A. Limiszewska, F. Hikmet, J. Huang, Y. Du, L. Lin, Z. Dong, L. Yang, X. Liu, H. Jiang, X. Xu, J. Wang, H. Yang, L. Bolund, A. Mardinoglu, C. Zhang, K. Von Feilitzen, C. Lindskog, F. Pontén, Y. Luo, T. Hökfelt, M. Uhlén, J. Mulder, An atlas of the protein-coding genes in the human, pig, and mouse brain. *Science* **367**, eaay5947 (2020).

41. T. E. Bakken, C. T. Van Velthoven, V. Menon, R. D. Hodge, Z. Yao, T. N. Nguyen, L. T. Graybuck, G. D. Horwitz, D. Bertagnolli, J. Goldy, A. M. Yanny, E. Garren, S. Parry, T. Casper, S. I. Shehata, E. R. Barkan, A. Szafer, B. P. Levi, N. Dee, K. A. Smith, S. M. Sunkin, A. Bernard, J. Phillips, M. J. Hawrylycz, C. Koch, G. J. Murphy, E. Lein, H. Zeng, B. Tasic, Single-cell and single-nucleus RNA-seq uncovers shared and distinct axes of variation in dorsal LGN neurons in mice, non-human primates, and humans. *eLife* **10**, e64875 (2021).

42. F. M. Krienen, M. Goldman, Q. Zhang, R. C. H. Del Rosario, M. Florio, R. Machold, A. Saunders, K. Levandowski, H. Zaniewski, B. Schuman, C. Wu, A. Lutservitz, C. D. Mullally, N. Reed, E. Bien, L. Bortolin, M. Fernandez-Otero, J. D. Lin, A. Wysoker, J. Nemesh, D. Kulp, M. Burns, V. Tkachev, R. Smith, C. A. Walsh, J. Dimidschstein, B. Rudy, L. S. Kean, S. Berretta, G. Fishell, G. Feng, S. A. McCarroll, Innovations present in the primate interneuron repertoire. *Nature* **586**, 262–269 (2020).

43. F. M. Krienen, K. M. Levandowski, H. Zaniewski, R. C. H. Del Rosario, M. E. Schroeder, M. Goldman, M. Wienisch, A. Lutservitz, V. F. Beja-Glasser, C. Chen, Q. Zhang, K. Y. Chan, K. X. Li, J. Sharma, D. McCormack, T. W. Shin, A. Harrahill, E. Nyase, G. Mudhar, A. Mauermann, A. Wysoker, J. Nemesh, S. Kashin, J. Vergara, G. Chelini, J. Dimidschstein, S. Berretta, B. E. Deverman, E. Boyden, S. A. McCarroll, G. Feng, A marmoset brain cell census reveals regional specialization of cellular identities. *Sci. Adv.* **9**, eadk3986 (2023).

44. T. Stuart, A. Butler, P. Hoffman, C. Hafemeister, E. Papalexi, W. M. Mauck, Y. Hao, M. Stoeckius, P. Smibert, R. Satija, Comprehensive Integration of Single-Cell Data. *Cell* **177**, 1888-1902.e21 (2019).

45. R. Liu, Z. Zhou, J. Huang, C. Chen, PMEPA1 promotes androgen receptor-negative prostate cell proliferation through suppressing the Smad3/4-c-Myc-p21 Cip1 signaling pathway. *J Pathol* **223**, 683–694 (2011).

46. I. Gritti, L. Mainville, B. E. Jones, Projections of GABAergic and cholinergic basal forebrain and GABAergic preoptic-anterior hypothalamic neurons to the posterior lateral hypothalamus of the rat. *J of Comparative Neurology* **339**, 251–268 (1994).

47. L. Heimer, R. E. Harlan, G. F. Alheid, M. M. Garcia, J. De Olmos, Substantia innominata: a notion which impedes clinical–anatomical correlations in neuropsychiatric disorders. *Neuroscience* **76**, 957–1006 (1997).

48. C. P. Bengtson, P. B. Osborne, Electrophysiological Properties of Cholinergic and Noncholinergic Neurons in the Ventral Pallidal Region of the Nucleus Basalis in Rat Brain Slices. *Journal of Neurophysiology* **83**, 2649–2660 (2000).

49. A. Lavin, A. A. Grace, Physiological properties of rat ventral pallidal neurons recorded intracellularly in vivo. *Journal of Neurophysiology* **75**, 1432–1443 (1996).

50. I. Mitrovic, T. C. Napier, Electrophysiological demonstration of mu, delta and kappa opioid receptors in the ventral pallidum. *J Pharmacol Exp Ther* **272**, 1260–1270 (1995).

51. T. C. Napier, I. Mitrovic, Opioid Modulation of Ventral Pallidal Inputs. *Annals of the New York Academy of Sciences* **877**, 176–201 (1999).

52. K. Pang, J. M. Tepper, L. Zaborszky, Morphological and electrophysiological characteristics of noncholinergic basal forebrain neurons. *J. Comp. Neurol.* **394**, 186–204 (1998).

53. M. R. Gielow, L. Zaborszky, The Input-Output Relationship of the Cholinergic Basal Forebrain. *Cell Reports* **18**, 1817–1830 (2017).

54. M. Sepp, K. Leiss, F. Murat, K. Okonechnikov, P. Joshi, E. Leushkin, L. Spänig, N. Mbengue, C. Schneider, J. Schmidt, N. Trost, M. Schauer, P. Khaitovich, S. Lisgo, M. Palkovits, P. Giere, L. M. Kutscher, S. Anders, M. Cardoso-Moreira, I. Sarropoulos, S. M. Pfister, H. Kaessmann, Cellular development and evolution of the mammalian cerebellum. *Nature* **625**, 788–796 (2024).

55. R. D. Hodge, T. E. Bakken, J. A. Miller, K. A. Smith, E. R. Barkan, L. T. Graybuck, J. L. Close, B. Long, N. Johansen, O. Penn, Z. Yao, J. Eggermont, T. Höllt, B. P. Levi, S. I. Shehata, B. Aevermann, A. Beller, D. Bertagnolli, K. Brouner, T. Casper, C. Cobbs, R. Dalley, N. Dee, S.-L. Ding, R. G. Ellenbogen, O. Fong, E. Garren, J. Goldy, R. P. Gwinn, D. Hirschstein, C. D. Keene, M. Keshk, A. L. Ko, K. Lathia, A. Mahfouz, Z. Maltzer, M. McGraw, T. N. Nguyen, J. Nyhus, J. G. Ojemann, A. Oldre, S. Parry, S. Reynolds, C. Rimorin, N. V. Shapovalova, S. Somasundaram, A. Szafer, E. R. Thomsen, M. Tieu, G. Quon, R. H. Scheuermann, R. Yuste, S. M. Sunkin, B. Lelieveldt, D. Feng, L. Ng, A. Bernard, M. Hawrylycz, J. W. Phillips, B. Tasic, H. Zeng, A. R. Jones, C. Koch, E. S. Lein, Conserved cell types with divergent features in human versus mouse cortex. *Nature* **573**, 61–68 (2019).

56. R. Fang, C. Xia, J. L. Close, M. Zhang, J. He, Z. Huang, A. R. Halpern, B. Long, J. A. Miller, E. S. Lein, X. Zhuang, Conservation and divergence of cortical cell organization in human and mouse revealed by MERFISH. *Science* **377**, 56–62 (2022).

57. T. E. Bakken, N. L. Jorstad, Q. Hu, B. B. Lake, W. Tian, B. E. Kalmbach, M. Crow, R. D. Hodge, F. M. Krienen, S. A. Sorensen, J. Eggermont, Z. Yao, B. D. Aevermann, A. I. Aldridge, A. Bartlett, D. Bertagnolli, T. Casper, R. G. Castanon, K. Crichton, T. L. Daigle, R. Dalley, N. Dee, N. Dembrow, D. Diep, S.-L. Ding, W. Dong, R. Fang, S. Fischer, M. Goldman, J. Goldy, L. T. Graybuck, B. R. Herb, X. Hou, J. Kancherla, M. Kroll, K. Lathia, B. van Lew, Y. E. Li, C. S. Liu, H. Liu, J. D. Lucero, A. Mahurkar, D. McMillen, J. A. Miller, M. Moussa, J. R. Nery, P. R. Nicovich, S.-Y. Niu, J. Orvis, J. K. Osteen, S. Owen, C. R. Palmer, T. Pham, N. Plongthongkum, O. Poirion, N. M. Reed, C. Rimorin, A. Rivkin, W. J. Romanow, A. E. Sedeño-Cortés, K. Siletti, S. Somasundaram, J. Sulc, M. Tieu, A. Torkelson, H. Tung, X. Wang, F. Xie, A. M. Yanny, R. Zhang, S. A. Ament, M. M. Behrens, H. C. Bravo, J. Chun, A. Dobin, J. Gillis, R. Hertzano, P. R. Hof, T. Höllt, G. D. Horwitz, C. D. Keene, P. V. Kharchenko, A. L. Ko, B. P. Lelieveldt, C. Luo, E. A. Mukamel, A. Pinto-Duarte, S. Preissl, A. Regev, B. Ren, R. H. Scheuermann, K. Smith, W. J. Spain, O. R. White, C. Koch, M. Hawrylycz, B. Tasic, E. Z. Macosko, S. A. McCarroll, J. T. Ting, H. Zeng, K. Zhang, G. Feng, J. R. Ecker, S. Linnarsson, E. S. Lein, Comparative cellular analysis of motor cortex in human, marmoset and mouse. *Nature* **598**, 111–119 (2021).

58. Y. Zhu, A. M. M. Sousa, T. Gao, M. Skarica, M. Li, G. Santpere, P. Esteller-Cucala, D. Juan, L. Ferrández-Peral, F. O. Gulden, M. Yang, D. J. Miller, T. Marques-Bonet, Y. Imamura Kawasawa, H. Zhao, N. Sestan, Spatiotemporal transcriptomic divergence across human and macaque brain development. *Science* **362**, eaat8077 (2018).

59. D. Villar, C. Berthelot, S. Aldridge, T. F. Rayner, M. Lukk, M. Pignatelli, T. J. Park, R. Deaville, J. T. Erichsen, A. J. Jasinska, J. M. A. Turner, M. F. Bertelsen, E. P. Murchison, P. Flicek, D. T. Odom, Enhancer evolution across 20 mammalian species. *Cell* **160**, 554–566 (2015).

60. J. Wang, H. Sun, M. Jiang, J. Li, P. Zhang, H. Chen, Y. Mei, L. Fei, S. Lai, X. Han, X. Song, S. Xu, M. Chen, H. Ouyang, D. Zhang, G.-C. Yuan, G. Guo, Tracing cell-type evolution by cross-species comparison of cell atlases. *Cell Rep* **34**, 108803 (2021).

61. D. Franjic, M. Skarica, S. Ma, J. I. Arellano, A. T. N. Tebbenkamp, J. Choi, C. Xu, Q. Li, Y. M. Morozov, D. Andrijevic, Z. Vrselja, A. Spajic, G. Santpere, M. Li, S. Zhang, Y. Liu, J. Spurrier, L. Zhang, I. Gudelj, L. Rapan, H. Takahashi, A. Huttner, R. Fan, S. M. Strittmatter, A. M. M. Sousa, P. Rakic, N. Sestan, Transcriptomic taxonomy and neurogenic trajectories of adult human, macaque, and pig hippocampal and entorhinal cells. *Neuron* **110**, 452-469.e14 (2022).

62. L. Geirsdottir, E. David, H. Keren-Shaul, A. Weiner, S. C. Bohlen, J. Neuber, A. Balic, A. Giladi, F. Sheban, C.-A. Dutertre, C. Pfeifle, F. Peri, A. Raffo-Romero, J. Vizioli, K. Matiasek, C. Scheiwe, S. Meckel, K. Mätz-Rensing, F. van der Meer, F. R. Thormodsson, C. Stadelmann, N. Zilkha, T. Kimchi, F. Ginhoux, I. Ulitsky, D. Erny, I. Amit, M. Prinz, Cross-Species Single-Cell Analysis Reveals Divergence of the Primate Microglia Program. *Cell* **179**, 1609-1622.e16 (2019).

63. Y. M. Kupchik, P. W. Kalivas, The rostral subcommissural ventral pallidum is a mix of ventral pallidal neurons and neurons from adjacent areas: an electrophysiological study. *Brain Struct Funct* **218**, 1487–1500 (2013).

64. R. Chen, T. R. Blosser, M. N. Djekidel, J. Hao, A. Bhattacherjee, W. Chen, L. M. Tuesta, X. Zhuang, Y. Zhang, Decoding molecular and cellular heterogeneity of mouse nucleus accumbens. *Nat Neurosci* **24**, 1757–1771 (2021).

65. H. Shi, Y. He, Y. Zhou, J. Huang, K. Maher, B. Wang, Z. Tang, S. Luo, P. Tan, M. Wu, Z. Lin, J. Ren, Y. Thapa, X. Tang, K. Y. Chan, B. E. Deverman, H. Shen, A. Liu, J. Liu, X. Wang, Spatial atlas of the mouse central nervous system at molecular resolution. *Nature* **622**, 552–561 (2023).

66. M. Zhang, X. Pan, W. Jung, A. R. Halpern, S. W. Eichhorn, Z. Lei, L. Cohen, K. A. Smith, B. Tasic, Z. Yao, H. Zeng, X. Zhuang, Molecularly defined and spatially resolved cell atlas of the whole mouse brain. *Nature* **624**, 343–354 (2023).

67. K. S. Smith, A. J. Tindell, J. W. Aldridge, K. C. Berridge, Ventral pallidum roles in reward and motivation. *Behav Brain Res* **196**, 155–167 (2009).

68. Y. M. Vachez, J. R. Tooley, K. Abiraman, B. Matikainen-Ankney, E. Casey, T. Earnest, L. M. Ramos, H. Silberberg, E. Godynyuk, O. Uddin, L. Marconi, C. E. Le Pichon, M. C. Creed, Ventral arkypallidal neurons inhibit accumbal firing to promote reward consumption. *Nat Neurosci* **24**, 379–390 (2021).

69. A. A. Prasad, G. P. McNally, The ventral pallidum and relapse in alcohol seeking. *British J Pharmacology* **177**, 3855–3864 (2020).

70. M. Engeln, M. E. Fox, R. Chandra, E. Y. Choi, H. Nam, H. Qadir, S. S. Thomas, V. M. Rhodes, M. D. Turner, R. J. Herman, C. A. Calarco, M. K. Lobo, Transcriptome profiling of the ventral pallidum reveals a role for pallido-thalamic neurons in cocaine reward. *Mol Psychiatry* **27**, 3980–3991 (2022).

71. L. Faget, L. Oriol, W.-C. Lee, C. Sargent, D. Ramanathan, T. S. Hnasko, “Ventral pallidum GABA and glutamate neurons drive approach and avoidance through distinct modulation of VTA cell types” (preprint, Neuroscience, 2023); https://doi.org/10.1101/2023.07.12.548750.

72. N. Bernat, R. Campbell, H. Nam, M. Basu, T. Odesser, G. Elyasaf, M. Engeln, R. Chandra, S. Golden, S. Ament, M. K. Lobo, Y. M. Kupchik, Multimodal interrogation of ventral pallidum projections reveals projection-specific signatures and effects on cocaine reward. *J. Neurosci.*, e1469232024 (2024).

73. L. A. Levi, K. Inbar, N. Nachshon, N. Bernat, A. Gatterer, D. Inbar, Y. M. Kupchik, Projection-Specific Potentiation of Ventral Pallidal Glutamatergic Outputs after Abstinence from Cocaine. *J. Neurosci.* **40**, 1276–1285 (2020).

74. Y.-W. Ji, Z.-L. Shen, X. Zhang, K. Zhang, T. Jia, X. Xu, H. Geng, Y. Han, C. Yin, J.-J. Yang, J.-L. Cao, C. Zhou, C. Xiao, Plasticity in ventral pallidal cholinergic neuron-derived circuits contributes to comorbid chronic pain-like and depression-like behaviour in male mice. *Nat Commun* **14**, 2182 (2023).

75. C. Zhu, Y. Yao, Y. Xiong, M. Cheng, J. Chen, R. Zhao, F. Liao, R. Shi, S. Song, Somatostatin Neurons in the Basal Forebrain Promote High-Calorie Food Intake. *Cell Rep* **20**, 112–123 (2017).

76. M. R. Farrell, C. M. Ruiz, E. Castillo, L. Faget, C. Khanbijian, S. Liu, H. Schoch, G. Rojas, M. Y. Huerta, T. S. Hnasko, S. V. Mahler, Ventral pallidum is essential for cocaine relapse after voluntary abstinence in rats. *Neuropsychopharmacology* **44**, 2174–2185 (2019).

77. J. A. Heinsbroek, D. N. Neuhofer, W. C. 3rd Griffin, G. S. Siegel, A.-C. Bobadilla, Y. M. Kupchik, P. W. Kalivas, Loss of Plasticity in the D2-Accumbens Pallidal Pathway Promotes Cocaine Seeking. *J Neurosci* **37**, 757–767 (2017).

78. A. R. Weiss, W. A. Liguore, K. Brandon, X. Wang, Z. Liu, J. S. Domire, D. Button, S. Srinivasan, C. D. Kroenke, J. L. McBride, A novel rhesus macaque model of Huntington's disease recapitulates key neuropathological changes along with motor and cognitive decline. *eLife* **11**, e77568 (2022).

79. A. R. Weiss, W. A. Liguore, J. S. Domire, D. Button, J. L. McBride, Intra-striatal AAV2.retro administration leads to extensive retrograde transport in the rhesus macaque brain: implications for disease modeling and therapeutic development. *Sci Rep* **10**, 6970 (2020).

80. W. A. Liguore, J. S. Domire, D. Button, Y. Wang, B. D. Dufour, S. Srinivasan, J. L. McBride, AAV-PHP.B Administration Results in a Differential Pattern of CNS Biodistribution in Non-human Primates Compared with Mice. *Molecular Therapy* **27**, 2018–2037 (2019).

81. L. Yang, I. Tochitsky, C. Woolf, W. Renthal, Isolation of Nuclei from Mouse Dorsal Root Ganglia for Single-nucleus Genomics. *BIO-PROTOCOL* **11** (2021).

82. Y. Hao, S. Hao, E. Andersen-Nissen, W. M. Mauck, S. Zheng, A. Butler, M. J. Lee, A. J. Wilk, C. Darby, M. Zager, P. Hoffman, M. Stoeckius, E. Papalexi, E. P. Mimitou, J. Jain, A. Srivastava, T. Stuart, L. M. Fleming, B. Yeung, A. J. Rogers, J. M. McElrath, C. A. Blish, R. Gottardo, P. Smibert, R. Satija, Integrated analysis of multimodal single-cell data. *Cell* **184**, 3573-3587.e29 (2021).

83. S. Durinck, Y. Moreau, A. Kasprzyk, S. Davis, B. De Moor, A. Brazma, W. Huber, BioMart and Bioconductor: a powerful link between biological databases and microarray data analysis. *Bioinformatics* **21**, 3439–3440 (2005).

84. S. Durinck, P. T. Spellman, E. Birney, W. Huber, Mapping identifiers for the integration of genomic datasets with the R/Bioconductor package biomaRt. *Nat Protoc* **4**, 1184–1191 (2009).

85. G. Paxinos, M. Keith B. J. Franklin, *The Mouse Brain in Stereotaxic Coordinates* (Elsevier Science, 2007; https://books.google.com/books?id=5MdpQgAACAAJ).

86. S. Berg, D. Kutra, T. Kroeger, C. N. Straehle, B. X. Kausler, C. Haubold, M. Schiegg, J. Ales, T. Beier, M. Rudy, K. Eren, J. I. Cervantes, B. Xu, F. Beuttenmueller, A. Wolny, C. Zhang, U. Koethe, F. A. Hamprecht, A. Kreshuk, ilastik: interactive machine learning for (bio)image analysis. *Nat Methods* **16**, 1226–1232 (2019).

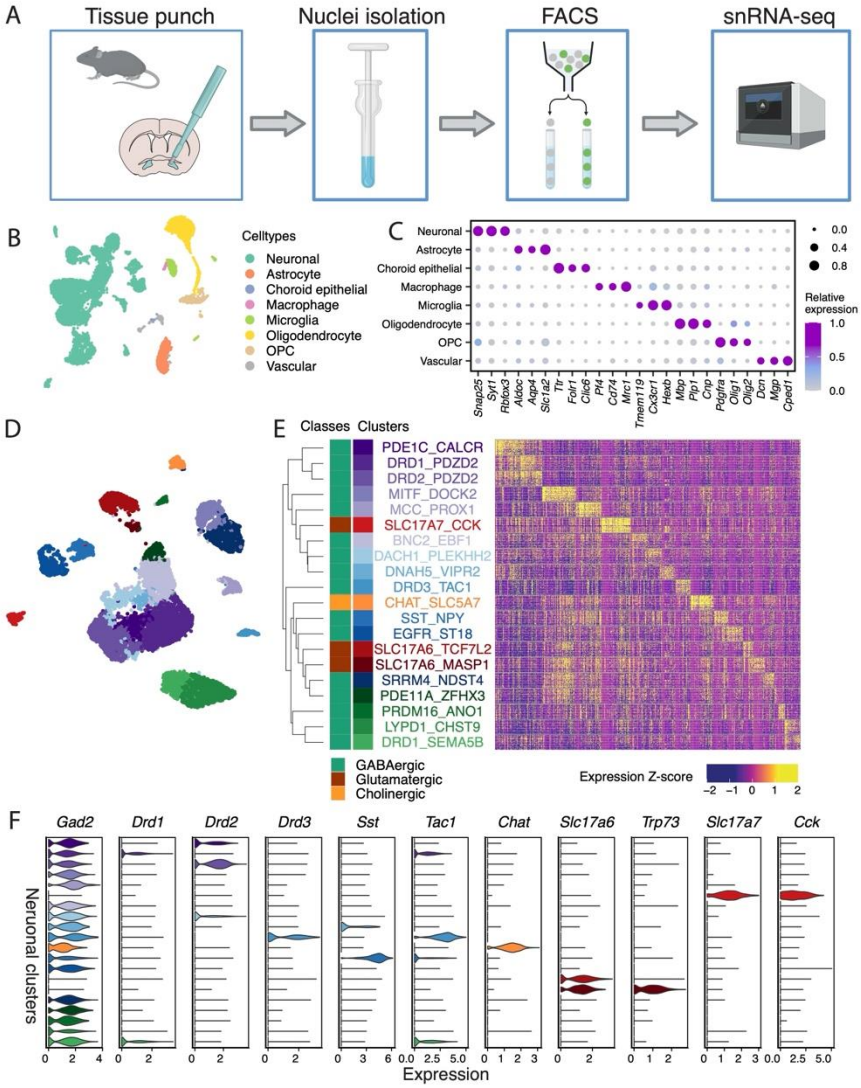

Fig. 1. Mouse atlas of ventral pallidum. (**A**) Experimental workflow of snRNA-seq of mouse VP. (**B**) Uniform manifold approximation and projection (UMAP) visualization of 10,000 downsampled nuclei, colored by cell types. (**C**) Dot plot displaying the expression of select cell-type-specific marker genes in individual cell types. Dot size denotes the fraction of nuclei expressing a marker gene (>0 counts), and color denotes relative expression of a gene in each cell type (calculated as the mean expression of a gene relative to the highest mean expression of that gene across all cell types). (**D**) UMAP of 10,000 downsampled mouse neuronal nuclei, colored by neuronal clusters. (**E**) Heatmap showing Z-scores of the expression of top 100 marker genes (sorted by Log2FC) per neuronal clusters in individual nuclei of snRNAs-seq. 50 nuclei are downsampled per neuronal cluster and displayed on the heatmap. Neuronal clusters are ordered based on the hierarchical clustering of the expression of marker genes displayed on the heatmap. The color bars on the side denote neuronal classes and clusters. (**F**) Violin plot showing log-transformed expression of select marker genes in individual neuronal clusters. Neuronal clusters are ordered according to the dendrogram in E.

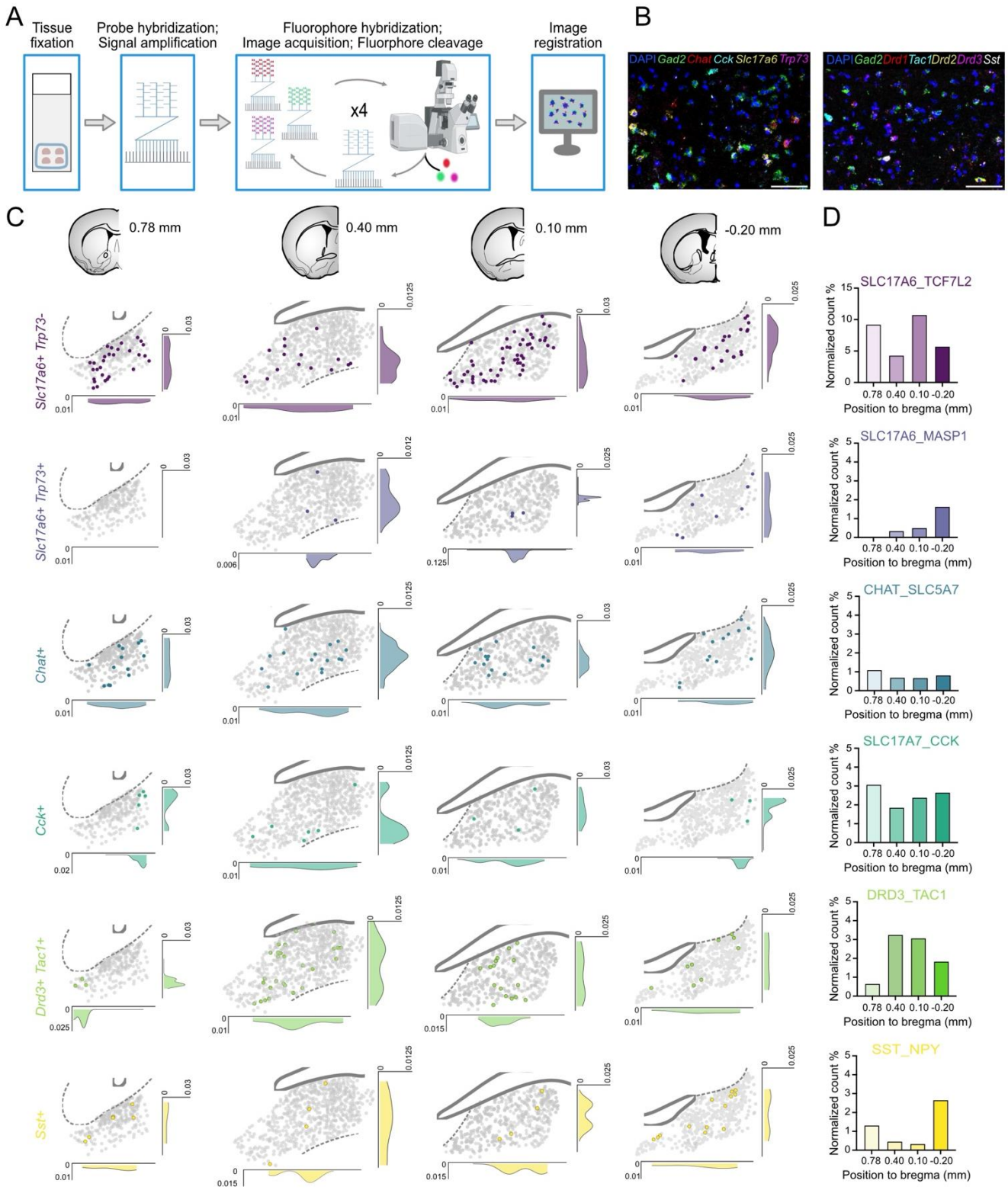

Fig. 2. Spatial organization of transcriptionally-distinct mouse clusters. (**A**) Experimental workflow of HiPlex FISH in mouse VP. (**B**) Representative HiPlex FISH images showing select probes for marker genes used to differentiate specific neuronal clusters. DAPI was used as a counterstain. Left: Probes hybridized to *Gad2*, *Chat*, *Cck*, *Slc17a6*, and *Trp73* mRNA. Right: Probes hybridized to *Gad2*, *Drd1*, *Tac1*, *Drd2*, *Drd3*, and *Sst* mRNA. Scale bar = 50 µm. (**C**) Spatial maps of neuronal clusters SLC17A6_TCF7L2, SLC17A6_MASP1, CHAT_SLC5A7, SLC17A7_CCK, DRD3_TAC1, and SST_NPY over four levels of the VP. Gene markers used to detect clusters are indicated to the left. Colorized dots represent cells that expressed marker genes for each specified cluster, while gray dots represent cells

that did not express these marker genes. Density plots depict the relative distribution of cells in individual clusters over the mediolateral and dorsoventral extent of the VP. (**D**) Bar graphs indicating the proportion of cells belonging to individual clusters over the anteroposterior axis of the VP. Counts for cells in each cluster were normalized to the total number of cells detected during HiPlex FISH at each level and expressed as a percentage.

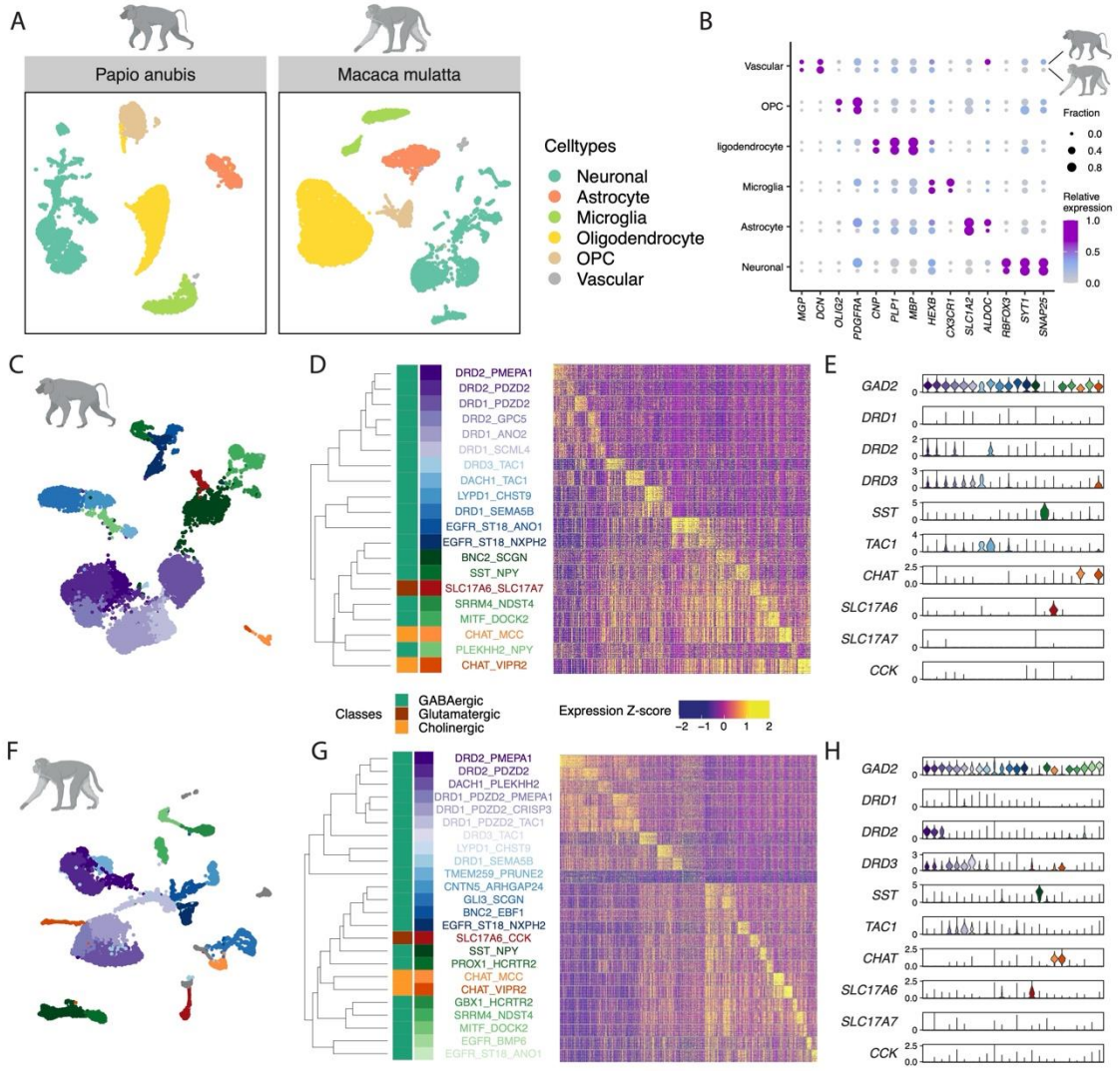

Fig. 3. Non-human primate atlas of ventral pallidum. (**A**) UMAP visualization of 10,000 downsampled nuclei each from baboon and macaque, colored by cell types. (**B**) Dot plot displaying the expression of select cell-type-specific marker genes in individual cell types from baboon and macaque. Dot size denotes the fraction of nuclei expressing a marker gene (>0 counts), and color denotes relative expression of a gene in each cell type (calculated as the mean expression of a gene relative to the highest mean expression of that gene across all cell types in the respective species). (**C** and **F**) UMAP of 10,000 downsampled neuronal nuclei from baboon (C) and macaque (F), colored by neuronal clusters. (**D** and **G**) Heatmap showing Z-scores of the expression of top 100 marker genes (sorted by Log2FC) per neuronal clusters in individual nuclei from baboon (D) and macaque (G). 50 nuclei per neuronal cluster are downsampled and displayed on the heatmap for each species. Neuronal clusters are ordered based on the hierarchical clustering of the expression of marker genes displayed on the heatmap. The color bars on the side denote neuronal classes and clusters. (**E** and **H**) Violin plot showing log-transformed expression of select marker genes in individual baboon (E) and macaque (H) neuronal clusters. Neuronal clusters are ordered according to the dendrogram in D and G, respectively.

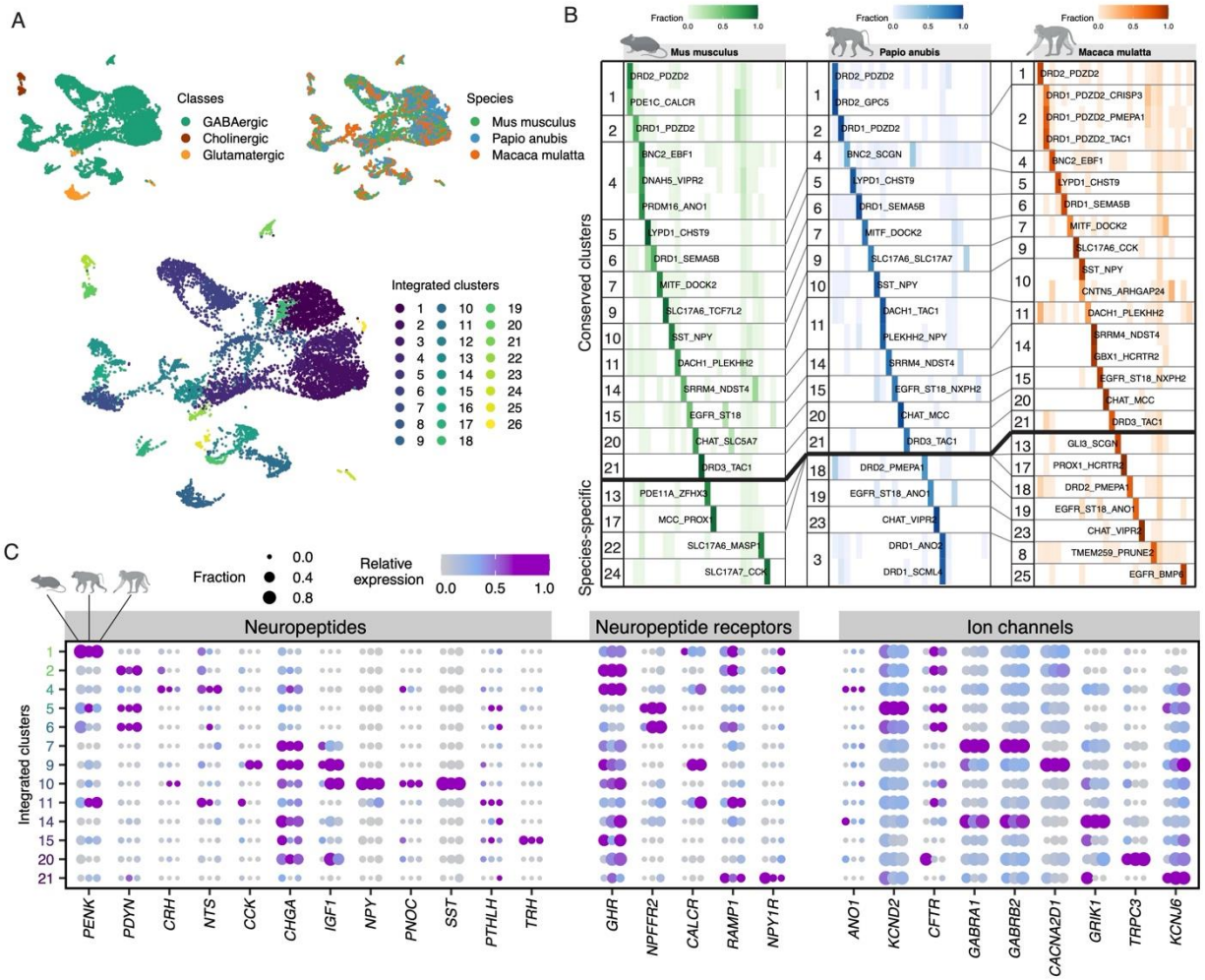

Fig. 4. Harmonized cross-species atlas of ventral pallidum neurons. (**A**) UMAPs of the harmonized neuronal atlas of VP. 3,000 neuronal nuclei per species are downsampled from mouse, baboon, and macaque. Nuclei are colored by neuronal cell types (top left), species (top right), and integrated clusters from the harmonized atlas (bottom). (**B**) Heatmap showing the correspondence of neuronal clusters across species. Fraction of nuclei in each neuronal cluster defined by independent analysis for each species that mapped to each integrated cluster identified in the harmonized atlas is calculated. Integrated clusters consisting of nuclei that made up over 30% of the nuclei from at least one neuronal cluster per species are considered conserved clusters. All other integrated clusters are identified as species-specific. (**C**) Dot plot displaying the expression of select gene panels in individual cell types from mouse, baboon, and macaque. Dot size denotes the fraction of nuclei expressing a marker gene (>0 counts), and color denotes relative expression of a gene in each cell type (calculated as the mean expression of a gene relative to the highest mean expression of that gene across all cell types in the respective species).

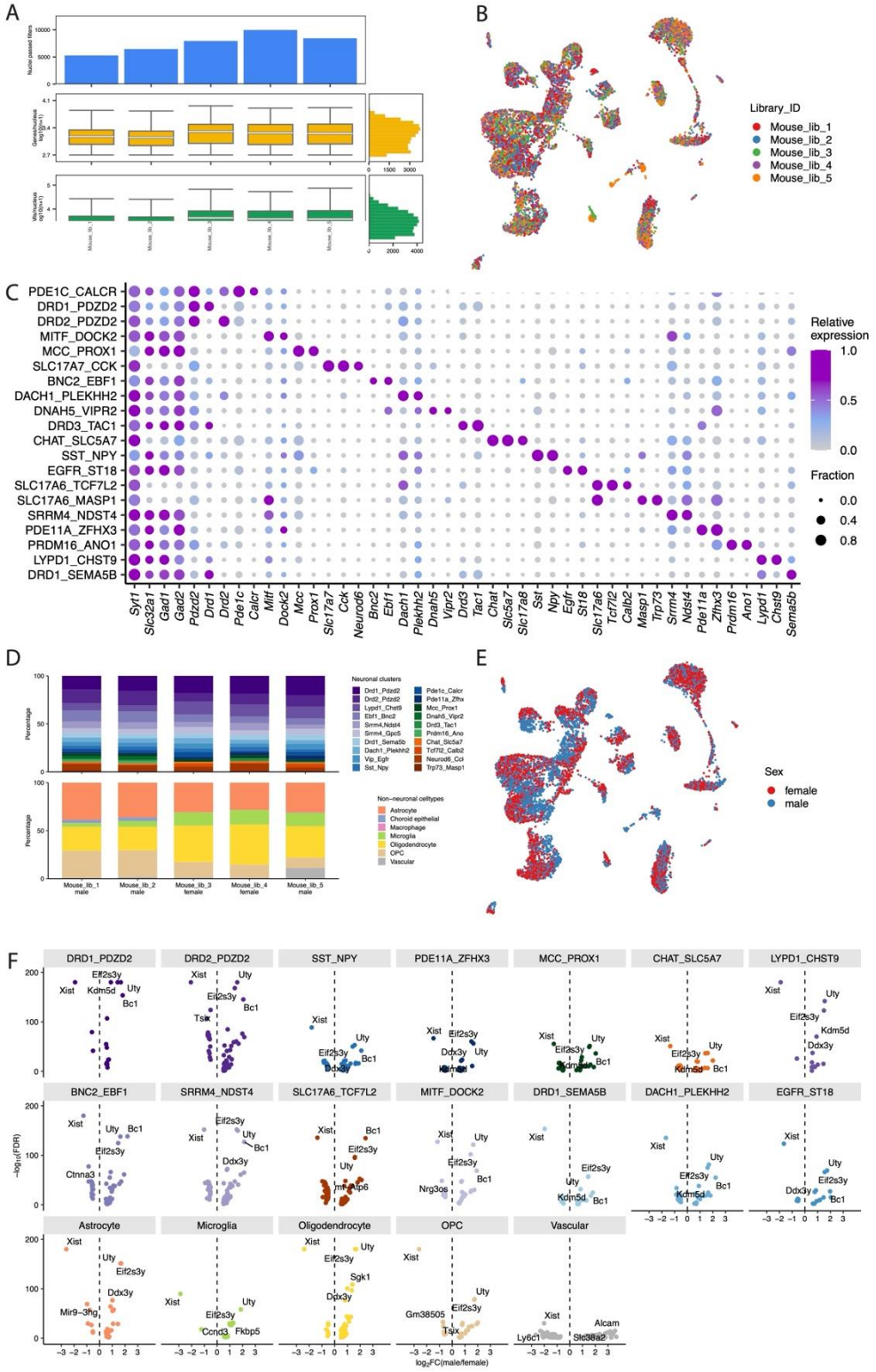

Fig. S1. Related to Fig. 1

(A) Mouse snRNA-seq library metrics. The top row displays the number of nuclei passed quality control. The middle row displays box plots of the number of genes per nucleus (log10 transformed) and the bottom row displays the number of UMIs per nucleus. Boxes indicate quartiles and whiskers are 1.5-times the interquartile range (Q1-Q3). The median is a white line inside each box. The distribution is aggregated across all samples and displayed on the horizontal histogram. (B) UMAPs of 2,000 downsampled mouse nuclei per library. Nuclei are colored by libraries. (C) Dot plot displaying the expression of marker genes for mouse neuronal clusters. Dot size denotes the fraction of nuclei expressing a marker gene (>0 counts), and color denotes relative expression of a gene in each cluster (calculated as the mean

expression of a gene relative to the highest mean expression of that gene across all clusters). (D) Stacked bar plot showing the composition of neuronal clusters (top) and non-neuronal cell types (bottom) in each mouse snRNA-seq library. (E) UMAPs of 5,000 downsampled mouse nuclei per sex. Nuclei are colored by sex. (F) Volcano plots of differentially expressed genes between nuclei from male (avg_log2FC > 0, FDR < 0.05) and female (avg_log2FC < 0, FDR < 0.05) in individual mouse cell types with at least 30 nuclei from each sex. The top 10 differentially expressed genes based on FDR are labeled.

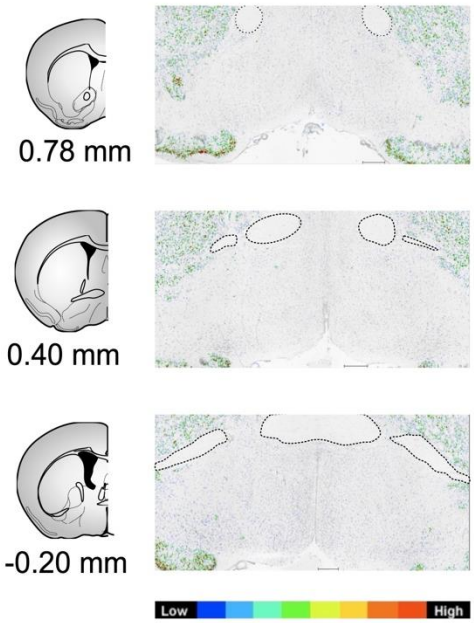

Fig. S2. *Pdzd2* expression in the mouse ventral pallidum – Related to Fig. 2

In situ hybridization data from the Allen Mouse Brain Atlas shows expression of Pdzd2 across the anteroposterior extent of the VP. Expression heatmap is overlaid. Scale bars = 300 µm. Allen Mouse Brain Atlas, https://mouse.brain-map.org/experiment/show/74988286.

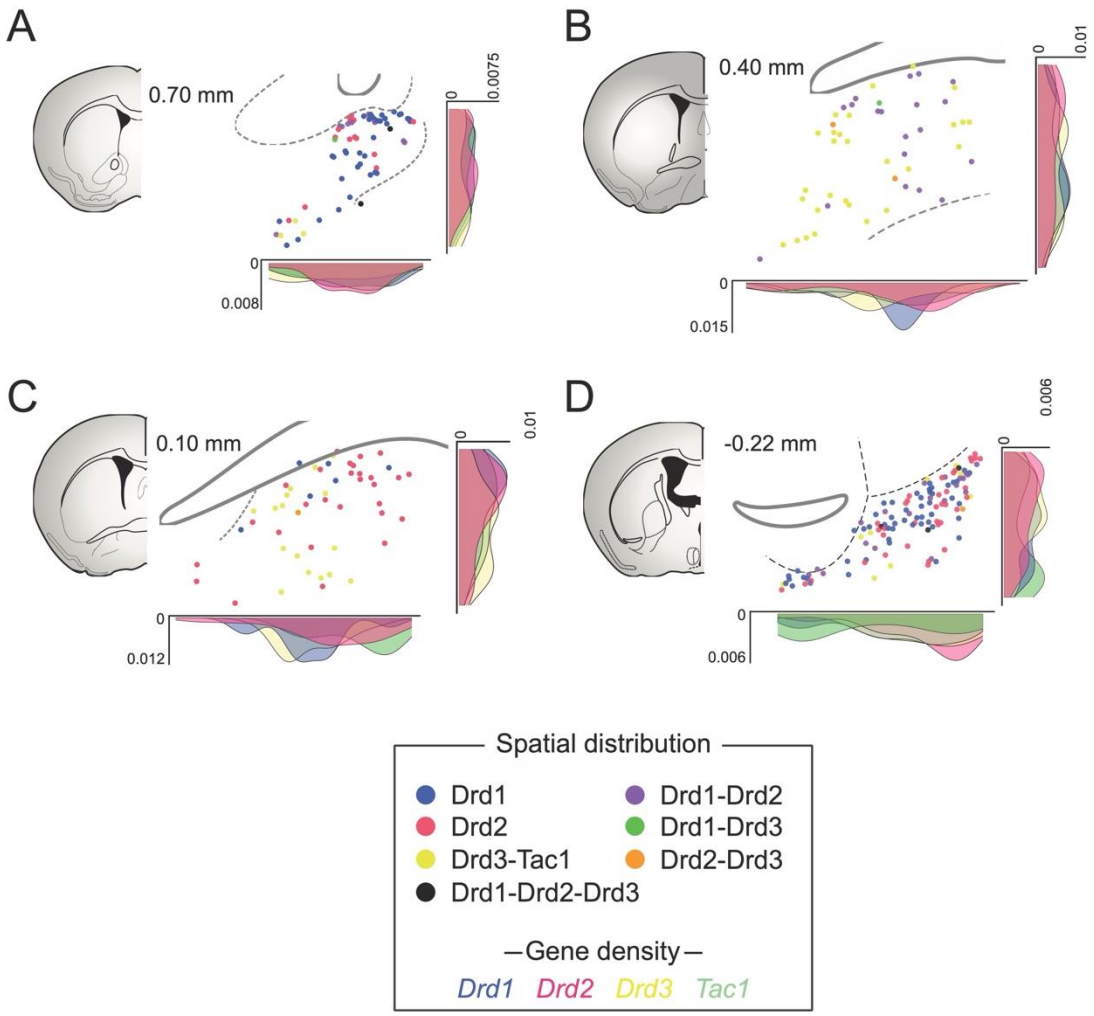

Fig. S3. Spatial organization of dopaminoceptive cells in the mouse ventral pallidum – Related to Fig. 2

Spatial maps of dopaminoceptive cells over four levels of the VP as determined by HiPlex FISH. Colorized dots correspond to cells that expressed probes that were hybridized to *Drd1*, *Drd2*, *Drd3*, and *Tac1* mRNA. Density plots depict the relative distribution of cells over the mediolateral and dorsoventral extent of the VP.

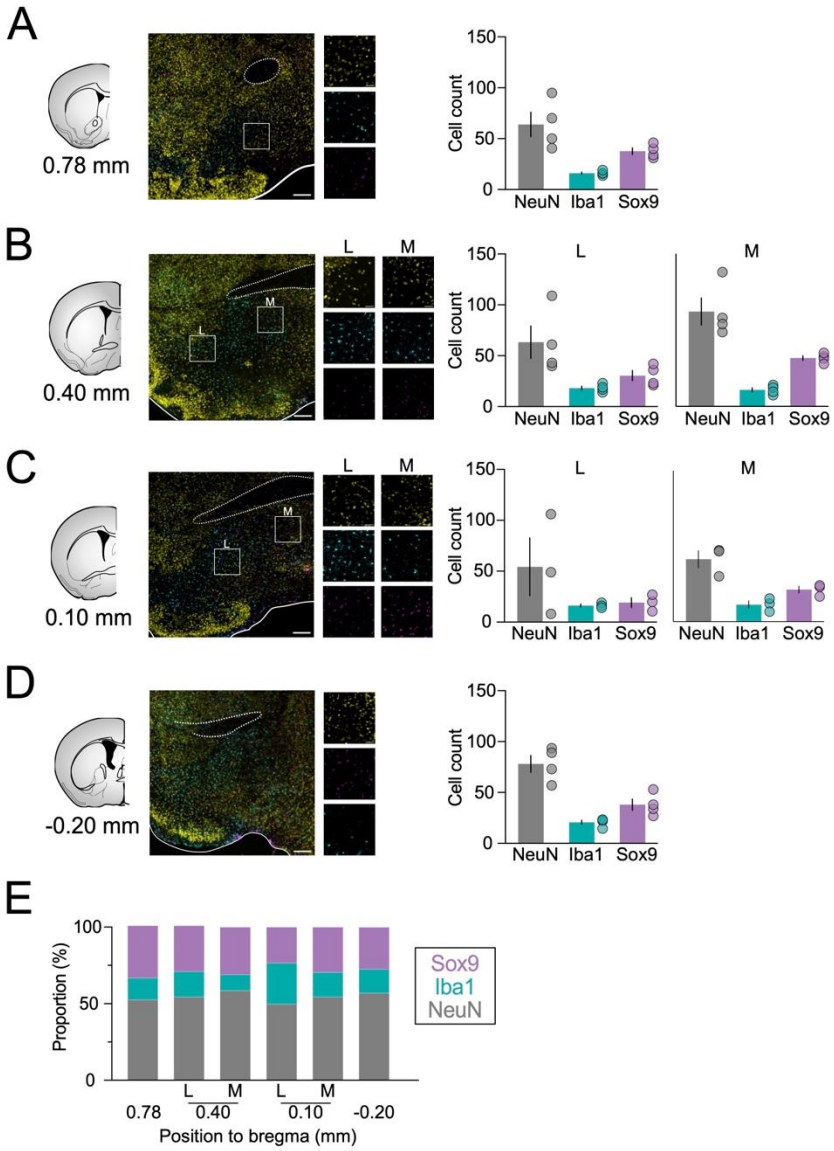

Fig. S4. Distribution of neuronal and non-neuronal cell types in the VP of mice – Related to Fig. 2

(A-D) (Left) Representative images of NeuN (yellow), Iba1 (cyan), and Sox9 (magenta) immunohistochemical staining over four levels, spanning the anterior-posterior extent of the VP. Low magnification image scale bar = 200 µm; high magnification image scale bar = 50 µm. (Right) The number of neurons (NeuN-positive), microglia (Iba1-positive), and astrocytes (Sox9) spatially distributed across the VP. (E) Stacked bar plot showing the relative proportion of neurons, microglia, and astrocytes at each defined level of the VP.

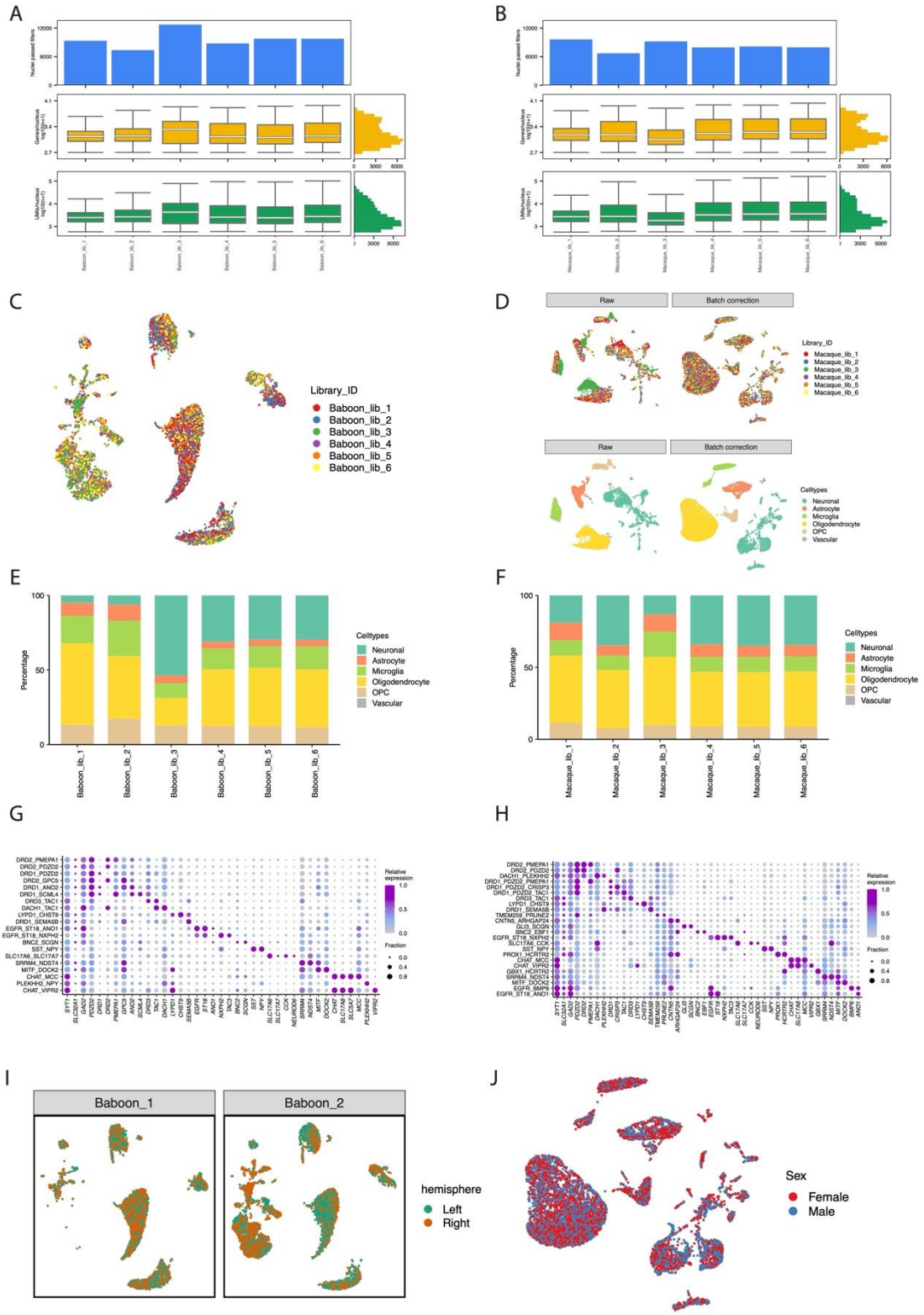

Fig. S5. Related to Fig. 3

snRNA-seq library metrics for baboon (A), and macaque (B). The top row displays the number of nuclei passed quality control. The middle row displays box plots of the number of genes per nucleus (log10 transformed) and the bottom row displays the number of UMIs per nucleus. Boxes indicate quartiles and whiskers are 1.5-times the interquartile range (Q1-Q3). The median is a white line inside each box. The distribution is aggregated across all samples and displayed on the horizontal histogram. (C) UMAPs of 2,000 downsampled baboon nuclei per library. Nuclei are colored by libraries. (D) Batch correction for the macaque dataset. 2,000 nuclei per library were randomly downsampled and shown on the UMAPs

pre- (left) and post-batch correction (right). Nuclei are colored by libraries (top) or celltypes (bottom). (E) and (F) Stacked bar plot showing the composition of neuronal clusters (top) and non-neuronal cell types (bottom) in each baboon (C), and macaque (D) snRNA-seq library. (G) and (H) Dot plot displaying the expression of marker genes for baboon (G) and macaque (H) neuronal clusters. Dot size denotes the fraction of nuclei expressing a marker gene (>0 counts), and color denotes relative expression of a gene in each cluster (calculated as the mean expression of a gene relative to the highest mean expression of that gene across all clusters). (I) UMAPs of 5,000 downsampled baboon nuclei per hemisphere per animal. Nuclei are colored by the origin of the hemisphere. (J) UMAPs of 5,000 downsampled macaque nuclei per sex. Nuclei are colored by sex.

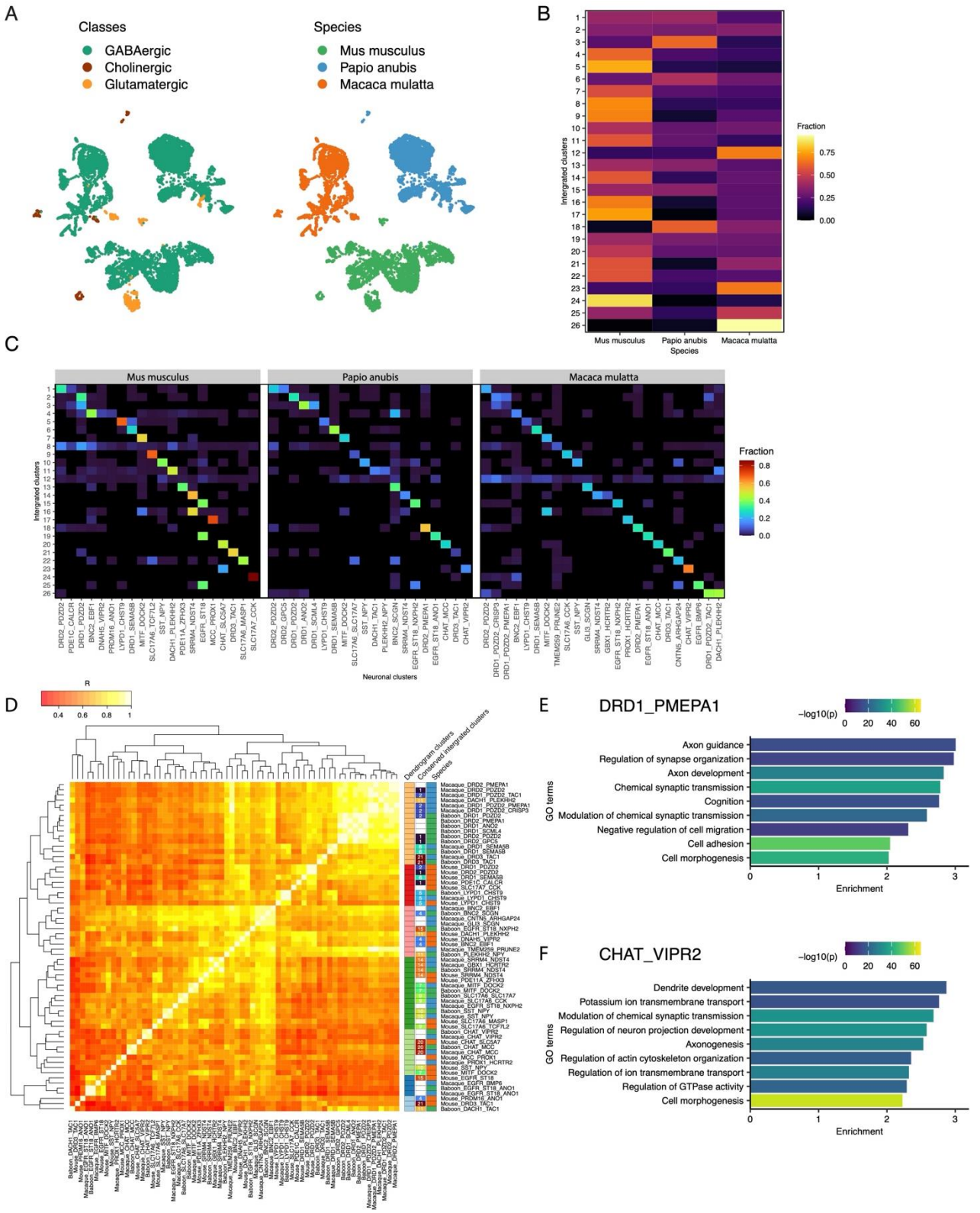

Fig. S6. Related to Fig. 4

(A) UMAPs showing the clustering of VP neuronal nuclei across species without integration. 3,000 neuronal nuclei per species are downsampled from mouse, baboon, and macaque. Nuclei are colored by neuronal cell types (top left), species (top right), and integrated clusters from the harmonized atlas (bottom). (B) Heatmap showing the fraction of nuclei in each integrated cluster by species. (C) Heatmap showing the fraction of nuclei in each integrated cluster by each neuronal cluster identified by independent analysis of each species. (D) Heatmap showing the Pearson's correlation coefficients of the

expression of conserved marker genes (Log2FC>0.5, FDR<0.05 in all species) across individual neuronal clusters identified by independent analysis of each species. Neuronal clusters are ordered based on the hierarchical clustering of the expression of conserved marker genes used in the heatmap. (E and F) Significant Gene Ontology terms enriched in shared marker genes (Log2FC>0.5, FDR<0.05 in both species) of DRD1_PMEPA1 and CHAT_VIPR2 clusters distinct in NHPs.

Abbreviation	**Full gene name**
ACVR1	activin a receptor, type 1
Calcr/CALCR	calcitonin receptor
Cck/CCK	cholecystokinin
Chat/CHAT	choline O-acetyltransferase
Dach1	dachshund family transcription factor
Ddx3y	dead box helicase 3, y-linked
DNAH5	dynein axonemal heavy chain 5
Drd1/DRD1	dopamine receptor D1
Drd2/DRD2	dopamine receptor D2
Drd3/DRD3	dopamine receptor D3
Ebf1/EBF1	early b cell factor 1 *(Mus musculus)*; BF transcription factor 1 (*Macaca mulatta, Papio anubis*)
Egfp/EGFP	epidermal growth factor receptor
FGF13	fibroblast growth factor 13
FOXN3	forkhead box n3
Gad1	glutamic acid decarboxylase 1
Gad2/GAD2	glutamic acid decarboxylase 2
GPC5	glypican 5
Htr1f	5-hydroxytryptamine (serotonin) receptor 1f
Lypd1/LYPD1	Ly6/Plaur domain containing 1 *(Mus musculus)*; LY6/PLAUR domain containing 1 (*Macaca mulatta, Papio anubis*)
MASP1	MBL associated serine protease 1
MCC	MCC regulator of WNT signaling pathway
Mitf	melanocyte inducing transcription factor
MOXD1	monooxygenase DBH like 1
NPY	neuropeptide y
NXPH2	neurexophilin 2
PDE1C	phosphodiesterase 1c
PDZD2	PDZ domain containing 2
PMEPA1	prostate transmembrane protein, androgen induced 1
Prdm16	PR domain containing 16
Prox1	prospero homeobox 1
Pvalb	parvalbumin
SEMA5B	semaphorin 5b
Slc17a6 /SLC17A6	solute carrier family 17, member 6 (vesicular glutamate transporter, isoform 2 [vGluT2])
Slc17a7/SLC17A7	solute carrier family 17, member 7 (vesicular glutamate transporter, isoform 1 [vGluT1])
Slc17a8/SLC17A8	solute carrier family 17, member 7 (vesicular glutamate transporter, isoform 3 [vGluT2])
Slc32a1/SLC32A1	solute carrier family 32, member 1 (gaba vesicular transporter 1)
SLC5A7	solute carrier family 5, member 7 (choline transporter)
SORCS3	sortilin related vps10 domain containing receptor 3

Srrm3	serine/arginine repetitive matrix 3
Sst/SST	somatostatin
St18	suppression of tumorigenicity 18 (*Mus musculus*); ST18 C2H2C-type zinc finger transcription factor (*Macaca mulatta*, *Papio anubis*)
Tac1/TAC1	tachykinin precursor 1
TAC3	tachykinin precursor 3
TCF7L2	transcription factor 7 like 2
Trp73	transformation related protein 73
Tsix	x inactive specific transcript, antisense
Ttr	transthyretin
Uty	ubiquitously transcribed tetratricopeptide repeat containing, y-linked
Vipr2/VIPR2	vasoactive intestinal peptide receptor 2
Xist	x inactive specific transcript
Zfhx3	zinc finger homeobox 3

Table. S1. List of gene names and abbreviations.